Preliminary Report on Polarimetric Calibration for the Advanced Technology Demonstrator

National Severe Storms Laboratory Report

prepared by: **Igor Ivić, Rafael Mendoza, David Schvartzman, Sebastian Torres, and Daniel Wasielewski**

November 2020

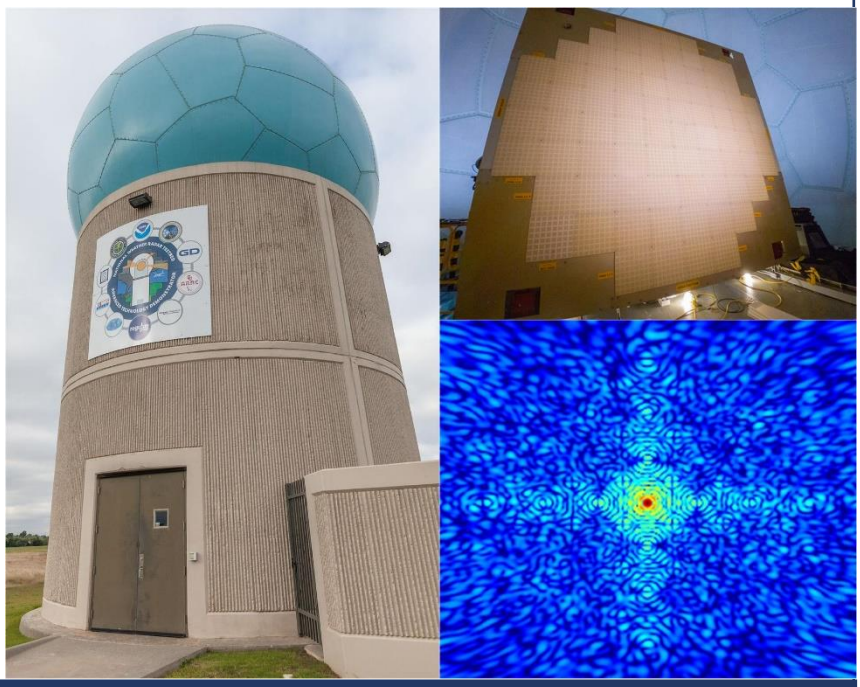

National Oceanic and Atmospheric Administration
National Severe Storms Laboratory
Norman, Oklahoma 73072

Executive summary

Phased array radar (PAR) technology is being considered as one of the candidates for the next generation of weather-surveillance radars in the US. The unique capabilities of this technology can potentially enable enhanced weather-surveillance strategies that could increase the quality and timeliness of weather radar products, ultimately improving severe-weather warnings and forecasts. One of the major technical challenges related to the use of PAR technology for weather surveillance is the integration of dual-polarization technology, which is currently available on the NEXRAD network, into polarimetric PAR (PPAR). In other words, a major condition for the adoption of PAR technology for weather surveillance is demonstrating that it can produce polarimetric radar variables that meet National Weather Service (NWS) requirements.

In polarimetric weather radars, the 1) copolar beam shape and channel matching, and 2) cross-polar isolation, primarily drive the quality of the polarimetric variables (i.e., differential reflectivity, differential phase, and copolar correlation coefficient). The copolar beam shape matching refers to the agreement between the location and size of radar resolution volumes sampled by the horizontally and vertically polarized radar beams. These are mainly controlled by the shape and the angular alignment of the copolar antenna radiation patterns (i.e., the directional dependence of the transmitted radio waves strength and the antenna directional sensitivity to radiation that impinges on it). The copolar channel matching refers to the similarities, both in amplitude and phase, between the transmit and receive electrical signals in the horizontal and vertical channels assuming perfectly spherical scatterers. If uncorrected, insufficient copolar channel matching leads to so-called "copolar biases" in the polarimetric variables. The cross-polar isolation measures the degree by which signals in the horizontal channel leak into the vertical channel, and vice versa; the higher the isolation (the smaller the leakage), the higher the quality of the polarimetric variables. This leakage occurs through the antenna cross-polar patterns on receive, as well as through the hardware in the antenna backplane receive paths, causing the so-called "cross-coupling biases" in the polarimetric variables. On PPARs, both the copolar beam/channel matching and the cross-polar isolation can drastically decrease when steering away from the antenna principal planes.

In general, polarimetric calibration consists of measuring the imperfections (i.e., mismatches and leakages) in the radar system and using these measurements to correct (or calibrate) the quantities measured by the radar. Unlike reflector antennas, which can be characterized by a single set of antenna radiation patterns and thus require a single set of calibration parameters, phased-array antennas employing electronic beamsteering exhibit different copolar and cross-polar antenna radiation patterns for each steering angle, and require a different set of calibration parameters for each. However, copolar beam shape mismatches cannot be corrected via polarimetric calibration in the real-time signal processor; thus, copolar beam shape matching must be achieved via precise beamforming. A satisfactory copolar channel matching can be achieved via corrections that require the measurement of the transmit and receive copolar beams. The cross-coupling biases can be reduced via the pulse-to-pulse phase-coding transmission scheme developed at NSSL without any calibration. However, the efficacy of this method declines as beams are steered farther away from the principal planes. For beamsteering directions where this method is insufficient, our

theoretical research suggests that the effects of signal leakage can be corrected using measurements of both the copolar and cross-polar beams.

The Advanced Technology Demonstrator (ATD) is a full-size, S-band, planar, proof-of-concept polarimetric PAR at the National Weather Radar Testbed (NWRT) in Norman, OK. Its main purpose is to serve as a testbed for evaluating the suitability of modern PPAR technology for weather observations. To support the measurements needed for calibration, we installed a Calibration Tower in the line of sight of the ATD. It provides a known source with a fixed geographical location that acts as a recognized "constant".

The ATD antenna was fully characterized in the near-field chamber at MIT-Lincoln Laboratory. We used these measurements to corroborate the need for corrections of the copolar and cross-coupling biases and the requirement of accurate characterization of copolar channel matching as well as cross-polar isolation. Because the cross-coupling biases can be effectively mitigated by using pulse-to-pulse phase-coding transmission schemes (at beamsteering angles corresponding to the lower elevations in a scan), the current ATD polarimetric calibration only corrects the beamsteering-dependent copolar biases associated with copolar channel mismatches.

Three off-line calibration processes were developed: (1) the absolute radar-cross-section (RCS) calibration, (2) the broadside polarimetric calibration, and (3) the beamsteering polarimetric calibration. The absolute RCS calibration uses the expected and measured reflectivities of the Calibration Tower to adjust the reflectivity calibration constant. The expected reflectivity of the Calibration Tower was empirically obtained by computing the ATD reflectivity calibration constant that minimized the differences between a field of KOUN radar reflectivity and a simultaneously collected field of ATD radar reflectivity. The broadside polarimetric calibration measures the copolar mismatches for all available transmission waveforms when the ATD beam is at broadside. This approach is analogous to the polarimetric calibration of a radar that uses a reflector antenna. The beamsteering polarimetric calibration measures the copolar mismatches relative to those at broadside when the ATD beam is electronically steered off broadside. For this process, copolar mismatches are measured for 341 electronically steered beam directions evenly distributed within the typical beamsteering coverage envelope; this takes ~4.5 hours. Additionally, a range-calibration process was developed to measure a range offset, which is defined as the difference between the actual range of the Calibration Tower and the range measured by the ATD. The ATD signal processor uses the stored outputs from these calibration processes to enable the application of corrections in real time.

Preliminary evaluation of the performance of the ATD polarimetric calibration was completed via a self-consistency test and with comparisons with neighboring WSR-88D radars. The self-consistency test relies on data from a series of sector scans obtained with the antenna in gradually different mechanical positions. As such, the data processing from a common sector between adjacent scans produces polarimetric variables for the same hydrometeors that are obtained with different electronic beamsteering angles. Thus, agreement in the data from one scan to the next confirms the performance of beamsteering polarimetric calibration. Our preliminary analyses show that the difference in the uncalibrated data from one scan to the next approximately match the expected biases obtained from the near-field antenna measurements. When calibrated, the agreement in the data from successive scans is significant, confirming the effectiveness of the current beamsteering polarimetric calibration.

Comparisons with other radars provide another means to evaluate the performance of the polarimetric calibration on the ATD. Similar qualitative and quantitative comparisons between WSR-88D data and ATD data both uncalibrated and calibrated provided very encouraging results that agreed with the results from the self-consistency test. At this time, however, we do not have enough data to precisely evaluate the accuracy of calibrated ATD polarimetric data using the described tests. Thus, it is still premature to make assessments as to whether the biases of the polarimetric variables meet NWS requirements.

Our evaluation identified two challenges. One challenge is related to system temperature drifts that affect the performance of the analog components in the antenna and ultimately compromise the repeatability and accuracy of some ATD calibration measurements. This is important because the entire polarimetric calibration takes several hours, and the system temperature can drift appreciably during this time. The observed temperature drifts may be exacerbated by the fact that the ATD antenna is air-cooled, so we are exploring improved thermal-management approaches for the ATD facility. We are also studying the relationship between the antenna temperature and the polarimetric calibration results to develop advanced processing of the calibration data that is more robust to temperature variations.

Another effect adversely affecting the repeatability and accuracy of polarimetric calibration measurements on the ATD is multipath interference. Multipath interference is a phenomenon whereby electromagnetic waves travel from their source to a detector via two or more propagation paths, and the two or more components of the resulting wave interfere constructively or destructively, introducing errors in the measurement of the direct-path signals. We speculate, however, that the multipath interference effects can be effectively mitigated via smoothing of the noisy measurements.

Once these two problems are addressed, we plan to focus on other important questions such as the stability and robustness of the polarimetric calibration process. The former will help us determine the frequency of execution for the off-line polarimetric calibration, while the latter will aid in identifying modifications to the current procedures or perhaps the development of different approaches.

To fully understand the performance of the ATD polarimetric calibration and assess the accuracy of the calibrated ATD polarimetric data, we will conduct self-consistency checks once a larger pool of ATD weather data is available, as well as conduct comparisons with the collocated WSR-88D radars. Another approach for data-quality assessment could involve the evaluation and comparison of Level III products obtained from the ATD base data. Additionally, we will research alternative calibration procedures. Of particular interest is the collaborative effort with the University of Oklahoma's Advanced Radar Research Center (ARRC) on the use of unmanned aerial systems for PPAR polarimetric calibration, which could be exploited to obtain more robust and practically feasible solutions to the PPAR polarimetric calibration problem. While not supported by the ATD, we also plan to continue collaboration with the ARRC to study the flexibility of the all-digital PPAR architectures. Such architectures significantly reduce the number of analog components and could lead to performance that is less susceptible to system temperature changes. Combined with liquid-cooling, these antenna architectures may result in more robust PPAR systems.

Despite all initial practical issues, it is our view that the current quality of the calibrated polarimetric data from the ATD is at a level sufficient for qualitative data interpretation at lower elevations. This finding was

verified via comparison with collocated WSR-88D radars and was corroborated by polarimetric radar experts outside of our group. We believe our preliminary results documented in this report suggest a promising outlook for our research and development efforts on the use of polarimetric phased-array radars for weather surveillance.

Table of Contents

1. Introduction

Polarimetric phased array radar (PPAR) technology is being considered as one of the candidates for the next generation of weather radars in the US (Zrnić et al. 2007, Weber 2019). This is reflected in numerous publications and conference presentations on the topic of PPAR use for weather observations (e.g., Panel Discussion: The Next-Generation Operational Weather Radar Network[1]). The unique electronic beam steering capability inherent in PPAR enables enhanced weather surveillance strategies that could improve the quality of weather radar products as well as reduce update times (Heinselman et al. 2011). However, one of the major challenges related to the use of PPAR technology for weather surveillance is the requirement to produce measurements with quality comparable to that from polarimetric parabolic-reflector antenna radars (PRAR) (Zrnić et al. 2012). This is typically referred to as the PAR-polarimetric-calibration challenge.

Unlike PRARs, PPAR antennas are characterized by significant cross-polar antenna patterns, which induce cross coupling between returns from the horizontally and vertically oriented fields, ultimately biasing polarimetric variable estimates. To address this issue, pulse-to-pulse phase coding in either the horizontal or vertical ports of the transmission elements has been proposed to mitigate the cross-coupling effects (Zrnić et al. 2014, Ivić 2017, Ivić 2017a, Ivić 2018a). This approach, however, does not address the scan-dependent biases in PPAR estimates that are a consequence of electronic beamsteering. These are caused by the horizontal (H) and vertical (V) copolar antenna patterns, which vary with beamsteering, and are referred to as copolar biases (or beamsteering biases if measured relative to a reference point such as broadside). The effects of these variations must be addressed by applying appropriate correction values at each boresight location (Ivić and Schvartzman 2019, Ivić and Schvartzman 2020). If the cross-coupling effects are sufficiently suppressed via phase coding, the corrections can be conducted using only the measurements of the copolar patterns (Ivić 2018b). However, the mitigation of cross-coupling effects achieved via pulse-to-pulse phase coding is inversely proportional to the cross-polar pattern levels. Thus, at boresight locations where the cross-polar pattern levels are relatively high (and the cross-coupling mitigation from phase coding is insufficient), a correction using knowledge of both the copolar and cross-polar patterns needs to be conducted (Ivić 2018). Furthermore, the effects of active electronic components in transmit and receive paths of PAR systems can result in significant differences between transmit and receive patterns. For these reasons, it is important to have an accurate characterization of both transmit as well as receive copolar and cross-polar antenna patterns (Ivić 2019) for effective polarimetric calibration of PPARs.

The Advanced Technology Demonstrator (ATD) is a full-size, S-band, planar, proof-of-concept PPAR at the National Weather Radar Testbed (NWRT) in Norman, OK (https://nssl.noaa.gov/tools/radar/atd/). Funded by the National Oceanic and Atmospheric Administration (NOAA) and the Federal Aviation Administration (FAA), the ATD was developed by the National Severe Storms Laboratory (NSSL), the University of Oklahoma (OU), MIT Lincoln Laboratory, and General Dynamics Mission Systems (Stailey and Hondl 2016). The main purpose of this system is to serve as a testbed for evaluating the suitability of modern PPAR technology for weather observations (Zrnić et al. 2007).

[1] https://ams.confex.com/ams/2019Annual/webprogram/Paper352287.html

In this preliminary report, we describe our efforts to date aimed at the polarimetric calibration of the ATD for weather measurements. We also identify remaining open questions and propose a plan for future research to determine whether PPARs can be adequately calibrated for weather observations and whether their calibration can be maintained over time. The ultimate goal is to determine if PPARs can produce weather radar products with quality that is commensurate with National Weather Service (NWS) requirements (NOAA/NWS RFR 2015).

The report is organized as follows. First, we describe the ATD hardware and its calibration infrastructure. Then, a bias assessment is conducted to familiarize the readers with the nature of biases in PPARs and to provide motivation for PPAR polarimetric calibration. The description of real-time software follows next. We continue by presenting weather-related polarimetric calibration procedures and their applications on weather data collected with the ATD. Finally, we end the report with a summary, conclusions, and a plan for future work.

2. The Advanced Technology Demonstrator (ATD)

2.1. Hardware

The ATD radar is composed of an Antenna Subsystem and Radar Backend Subsystem installed on an Elevation Pedestal and an Azimuth Turntable to allow mechanical positioning (Figure 2.1.1). The radar is installed atop a 10 m tower and enclosed within a spherical radome.

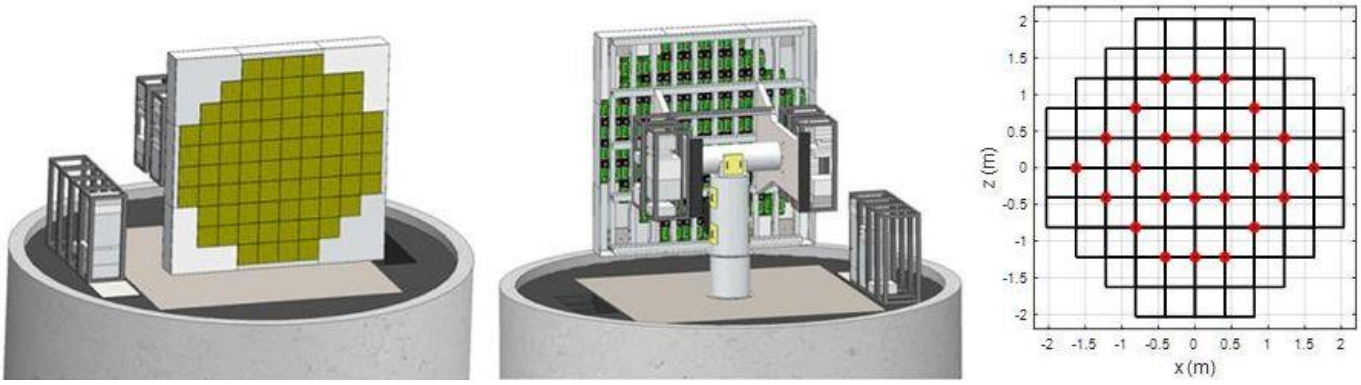

Figure 2.1.1. Front (left panel) and back (middle panel) of the antenna assembly. The antenna layout with subarray centers shown as red dots (right panel).

The Antenna Subsystem consists of the antenna and a processor referred to as the Beam Steering Generator (BSG). The antenna is a 4-m Active Electronically Scanned Array (AESA) with individual active Transmit/Receive modules for each of the 4864 elements. It consists of 76 panels, each with an 8x8 matrix of dual-polarization (horizontal and vertical) radiating elements. Electronic steering is controlled by phase shifters at the element level. Low-level control of the phase shifters and transmit/receive amplifiers on a panel is handled by a Field Programmable Gate Array (FPGA), which receives higher-level instructions from the BSG.

On receive, the signals from the 64 elements of each panel are first internally summed. Each of the 76 panels provides four outputs (i.e., two in H and two in V) in support of the overlapped subarray architecture

employed by the ATD (Herd et al. 2005). Each subarray consists of 8 panels arranged in a 2×4 matrix for a total of 24 subarrays in H and 24 in V. The antenna layout and subarray centers are shown in Figure 2.1.1.

The Radar Backend Subsystem is located on the yoke arms of the elevation pedestal and comprises all the equipment responsible for waveform generation and downconversion/digitization of the received echoes. The Digital Receiver/Exciter cabinet generates the radar signal at the chosen center frequency, along with the desired waveform, all timing signals necessary for the radar signal processing, and the local oscillator for downconversion of the RF to a lower intermediate frequency (IF) for digitization. The Analog Receiver subassembly within the Radar Backend primarily handles the analog RF signals from the antenna, which have already been summed analogously into 48 subarray signals (24 for H and 24 for V) + 2 sidelobe blanker channels. These 50 signals are downconverted from RF to IF prior to digitization and processing. The Digital Beamformer within the Radar Backend serves as the first level of processing, combining the digitized subarray data, applying digital beamforming, and retaining the beam data only.

The Antenna and Radar Backend Subsystems are both located on an Elevation Pedestal and Azimuth Turntable. The Elevation Pedestal provides mechanical positioning of the antenna from -1° to 181° (upside-down on the reverse side). The Azimuth Turntable can move through the full 360°. Both are primarily intended for positioning the antenna to scan electronically, but the Azimuth Turntable may be rotated continuously if desired. The polarimetric calibration schemes described later in this report make use of mechanical positioning to characterize the beam at various electronic steering angles.

Nearfield testing of the ATD antenna was conducted by the MIT-Lincoln Laboratory prior to installation in Norman, OK (Conway et al. 2018). During this testing, multiple parameters were measured such as EIRP (Equivalent Isotropic Radiated Power), broadside directivity, beamwidth, beam steering accuracy, mean squared sidelobe level (MSSL), and cross-polarization isolation. The results are summarized in Table 2.1.1.

Table 2.1.1. ATD nearfield testing results.

Antenna Metric	**Goal**	**Measured**
EIRP	85.4 dBW	85.3 dBW TxV 84.8 dBW TxH
Broadside Directivity	41.1 dB (Rx) 42.3 dB (Tx)	40.8 dB (Rx) 41.9 dB (Tx)
Relative EIRP, Gain between V& H Beams	< 0.1 dB delta between V and H	0.5 dB delta between V and H
Beamwidth	1.8° (Rx), 1.4° (Tx)	1.7° (Rx), 1.3° (Tx)
Mean Squared Sidelobe Level (MSSL)	< -50 dB	-53.9 dB (RxV) -53.1 dB (RxH) -50.4 dB (TxV) -49.3 dB (TxH)
Beampoint Error	< 0.05°	< 0.04°
Cross Pol Isolation	> 35dB	> 35 dB (Rx) > 40 dB (Tx)

To increase the sensitivity, the ATD employs pulse compression and a matched receiver filter that results in range resolution that is several times better than the length of the transmitted pulse. This approach, however, results in a considerable blind range that depends on the length of the transmitted pulse. To resolve this issue, the ATD transmits a short "fill" pulse immediately after the phase-modulated long pulse. The two pulses are shifted by 8 MHz relative to the center operating frequency, and the corresponding returns are separated via filtering in the digital receiver. The sampling rates on the "long" and "short" pulse channels are 8 and 4 MHz, respectively. After applying the pulse-compression matched filter, the "long" pulse data are decimated to a sampling rate of 4 MHz. Thus, four streams of IQ signals with 4-MHz sampling are sent to the weather Digital Signal Processor (DSP): the H-polarization "long" and "short" pulse data and the V-polarization "long" and "short" pulse data. The range sampling spacing for these signals is 37.5 m.

2.2. Calibration Infrastructure

The ATD is installed within the repurposed NWRT facility in Norman, OK. Before this installation, a Calibration Tower was installed north of the ATD. The overall purpose of the Calibration Tower is to provide a means for numerous calibrations and system checks needed for proper ATD operation. Prior to its arrival in Oklahoma, the ATD antenna was characterized in the near-field chamber at MIT Lincoln Laboratory. The Calibration Tower provides a complementary capability with an external, open-air, far-field test range.

Figure 2.2.1. The ATD Calibration Tower.

The Calibration Tower (Figure 2.2.1) is 45-m tall and is located approximately 425 m north of the ATD. Affixed upon the top of the Calibration Tower is a Radome assembly that houses a standard single-polarization gain horn on a motorized rotating platform. The Calibration Tower horn is an S-band WR-284 standard gain horn that has a nominal antenna gain of 10 dB. The horn is connected to a remotely controllable servo motor that can change its orientation between horizontal, vertical, or any other desired position. The primary purpose of the Calibration Tower horn is to transmit and receive test signals to and from the ATD antenna. At the base of the tower is an enclosure containing RF circuitry that supports six different modes of operation with coherent RF signal paths to and from the ATD radar. It can also transmit an independent, non-coherent, continuous-wave signal. Underground single-mode optical-fiber transmission lines carry RF and Ethernet signals between the ATD and Calibration Tower.

The ATD Facility houses the command and control of the Calibration Tower equipment. A processor called the Calibration Tower Controller receives mode requests from the ATD software and performs the necessary actions on the Calibration Tower RF Circuit to support the desired mode (transmit with the full array, transmit with a single element, receive with ATD antenna, loopback, etc.).

In summary, the ATD calibration tower provides a known, coherent source with a fixed geographical location that acts as a recognized “constant” to support the ATD polarimetric calibration.

Figure 2.2.2. The ATD Facility and the Calibration Tower.

2.3. Preliminary Bias Assessment

As mentioned before, before installation at the NWRT, the ATD antenna transmit and receive copolar and cross-polar patterns were measured in the near-field chamber at the MIT-Lincoln Laboratory facilities in March-April 2018 (Conway et al. 2018). The patterns were collected for a total of 2,859 electronic beamsteering positions. Beam peaks were extracted from each measured copolar and cross-polar pattern, and results are shown in Figure 2.3.1 (left and middle panels). The extracted beam peaks effectively produce average embedded radiation element patterns. These element patterns can be coupled with the theoretically computed array factor (i.e., a directional two-dimensional function that weights the pattern shapes of individual radiators via controlling the relative phases and amplitudes of the radio waves emitted by the antenna elements in the array) to produce realistic ATD antenna patterns that account for the variable array impedances, the pattern shapes of individual radiators as well as mutual coupling among them. Furthermore, by extracting copolar beam peaks along the horizontal cardinal plane, the copolar biases for reflectivity in H (Z_h), differential reflectivity (Z_{DR}), and differential phase (Φ_{DP}) can be computed and are shown in the right panels of Figure 2.3.1 (note that the biases are normalized to broadside). To put this into perspective, it is desirable that the bias of Z estimates is kept within ±1 dB and that of Z_{DR} estimates within ±0.1 dB for intrinsic (i.e., true) Z_{DR} between 0 and 1 dB and less than $\pm 0.1 \times Z_{DR}$ for larger Z_{DR} values (Zrnić et al. 2010, NOAA/NWS RFR 2015). However, the biases shown in this figure significantly exceed the desired limits, especially as the beamsteering angles depart from broadside (0° in azimuth and elevation). These results corroborate the need for corrections of beamsteering biases (i.e., calibration) that require accurate characterization of copolar pattern levels relative to each other. In addition, relative phases of copolar patterns must be measured to correct for (calibrate) differential phase changes as beams are steered in various directions to meet the bias limit requirement of ±1° (NOAA/NWS RFR 2015).

In addition, using the ATD antenna patterns (created using measured embedded ATD element patterns coupled with the array factor), the cross-coupling biases of polarimetric variables can also be computed using analytical expressions in Ivić (2017). Figure 2.3.2 shows cross-coupling biases for beams directed at *az* = 0°, *el* = 30° and *az* = 30°, *el* = 15°. The biases are computed for Simultaneous Transmission Simultaneous Reception (STSR) and Phase Coded Simultaneous Transmission Simultaneous Reception (PCSTSR) modes. These indicate that the cross coupling can also cause biases that exceed the desired limits and that these biases increase as beams are electronically steered away from the H and V principal planes. As shown in Figure 2.3.2, these biases strongly depend on the intrinsic value of Φ_{DP}. Also, the results for PCSTSR mode demonstrate that the pulse-to-pulse phase coding effectively mitigates cross-coupling biases in Z_{DR} and Φ_{DP} estimates but exacerbates them in $|\rho_{hv}|$ estimates (bottom middle panel in Figure 2.3.2). To put the bias of $|\rho_{hv}|$ estimates in perspective, note that Balakrishnan and Zrnić (1990) state that biases within ±0.01 should be sufficient for "*sensing the mixed-phase precipitation and gauging the hail size quantitatively*". At the same time, NOAA/NWS radar functional requirements (NOAA/NWS RFR 2015) set the bias limits for $|\rho_{hv}|$ estimates to an even more stringent value of ±0.006. In that regard, the black curve in the lower middle panel of Figure 2.3.2 shows significant biases in $|\rho_{hv}|$ estimates exceeding the recommended limits for intrinsic Φ_{DP} values larger than ~50° in the PCSTSR mode. For Φ_{DP} estimates, the

bias limit requirement of ±1° is exceeded in both the STSR and PCSTSR modes at *az* = 30°, *el* = 15° (lower right panel in Figure 2.3.2), but not at *az* = 0°, *el* = 30° (upper right panel in Figure 2.3.2).

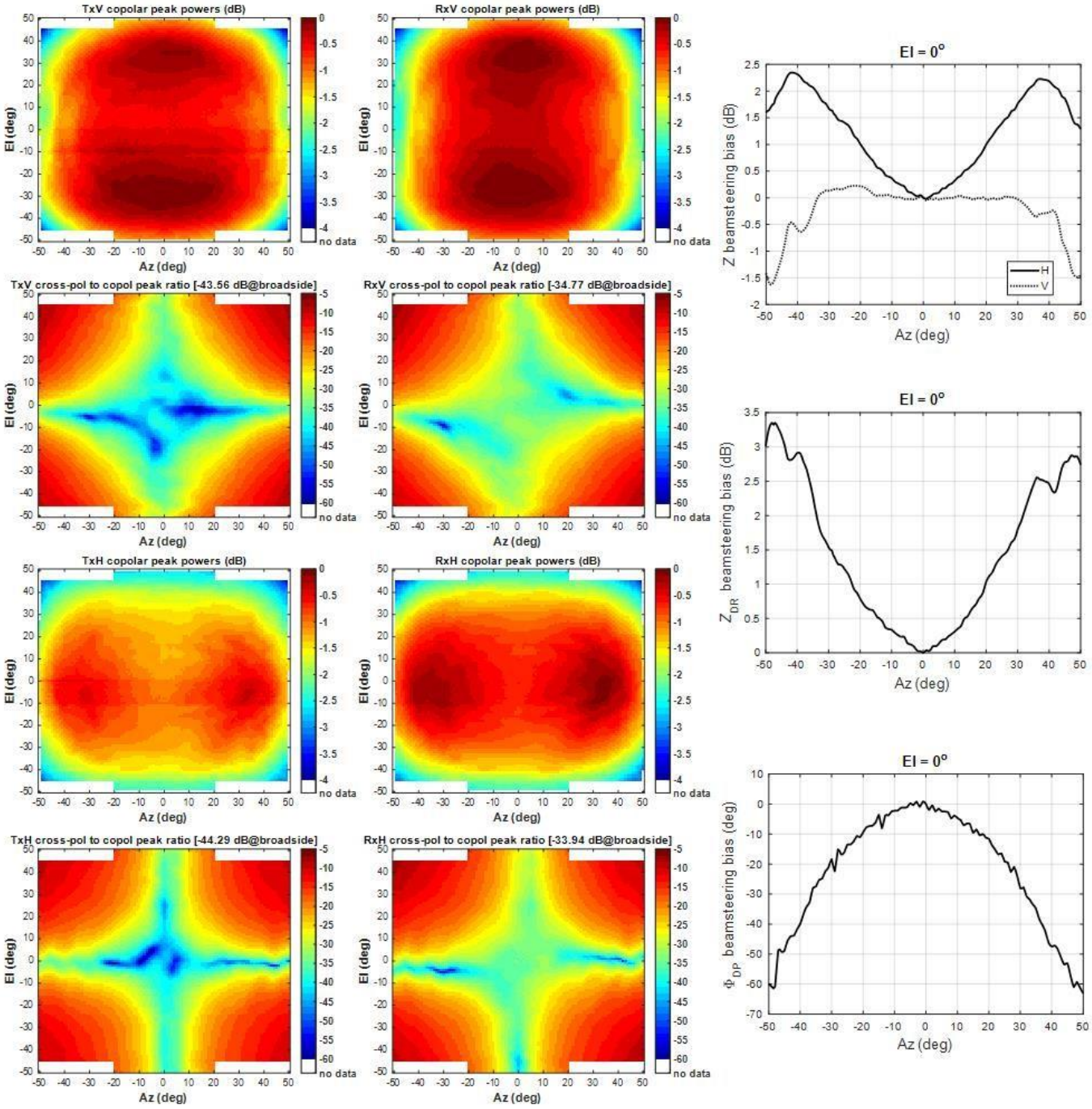

Figure 2.3.1. Transmit (left panels) and receive (middle panels) beam peak powers of the ATD antenna measured in the near-field chamber. Near-field derived beamsteering *biases along the horizontal principal plane (right panels).*

Overall, two approaches may be applied to mitigate the copolar and cross-coupling biases. The first approach is to collect data in the PCSTSR mode and correct only copolar biases. This simpler approach works well for beam directions where pulse-to-pulse phase coding sufficiently mitigates cross-coupling

biases. For beam directions where this is not the case, a second more involved approach is required utilizing knowledge of both copolar and cross-polar patterns.

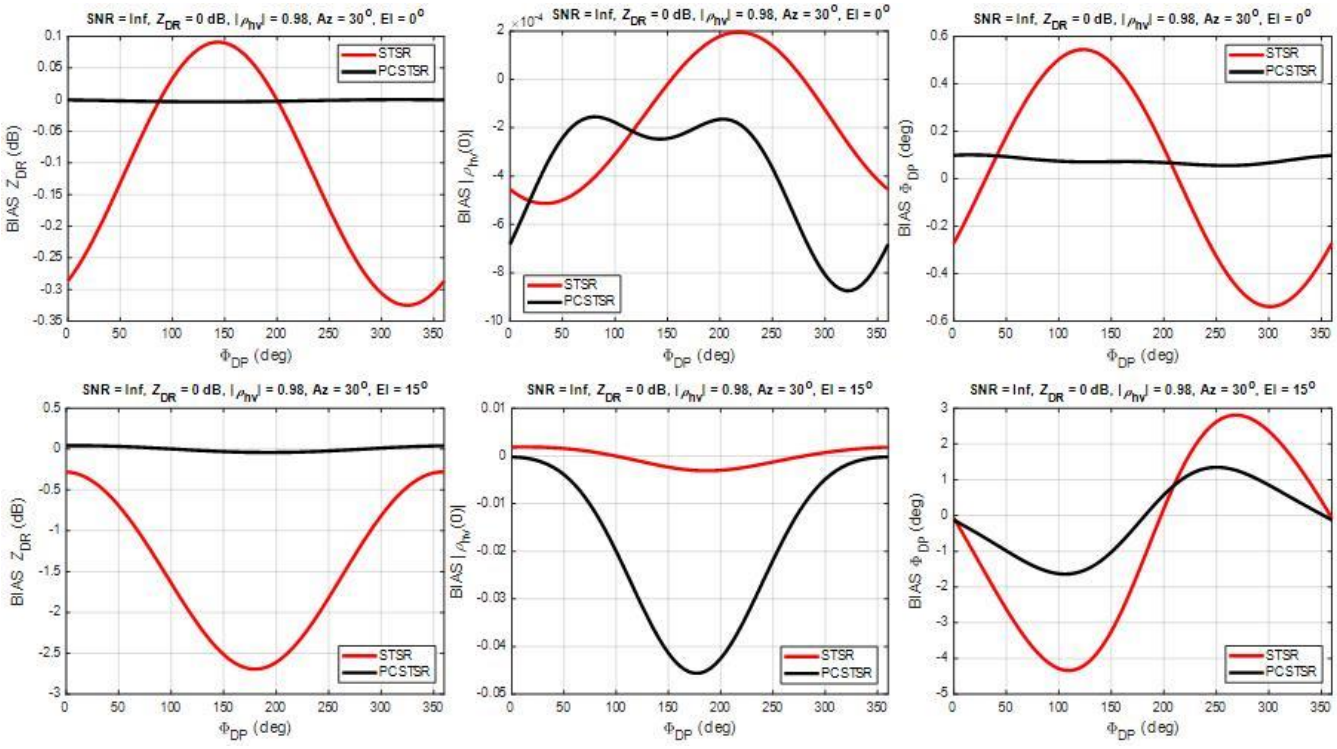

Figure 2.3.2. Cross-coupling biases in polarimetric variable estimates for az = 0°, el = 30° (upper panels) and az = 30°, el = 15° (lower panels).

2.4. Application Software: Radar Control/Monitoring and Signal Processing

The Application Software in the ATD includes two signal-processing paths (one for the Air-Traffic Control mission, or ATC-DSP, and one for Weather Surveillance mission, or Wx-DSP) and two human-machine interfaces, or HMIs (the General Dynamics HMI, or GD-HMI, and the NSSL/CIMMS Weather HMI, or Wx-HMI). The GD-HMI controls the back end of the radar, commands other subsystems (such as the BSG), and can be used to configure and execute ATD calibration sequences. When a calibration sequence is executed successfully from the GD-HMI, calibration products (the outputs obtained from processing the calibration data) are sent to the Wx-DSP. The Wx-DSP receives calibration products and stores them in the so-called Product Database. The latest available calibration products are loaded by the Wx-DSP and used in real-time data processing (e.g., when collecting weather data). Furthermore, archived calibration products can be used to conduct a historical analysis of the stability and accuracy of the polarimetric calibration on the ATD. Also, through the systematic analysis of archived calibration products, we plan to continue to enhance calibration sequences for improved stability and robustness.

The Wx-HMI is designed to support weather data collection activities. Figure 2.4.1 illustrates the main control panel in the Wx-HMI. The system tab displays high-level control parameters and allows a user to start a weather data collection. The top section has clickable buttons used to enable/disable subsystems and/or specific functionality. For example, the base data (Level-II) and time-series data (Level-I) can be recorded by clicking on the “Base Data” and “IQ Data” buttons in the “Application Software” panel,

respectively. The bottom section displays important notifications that inform the user of the state of the radar (e.g., status information, warnings, errors).

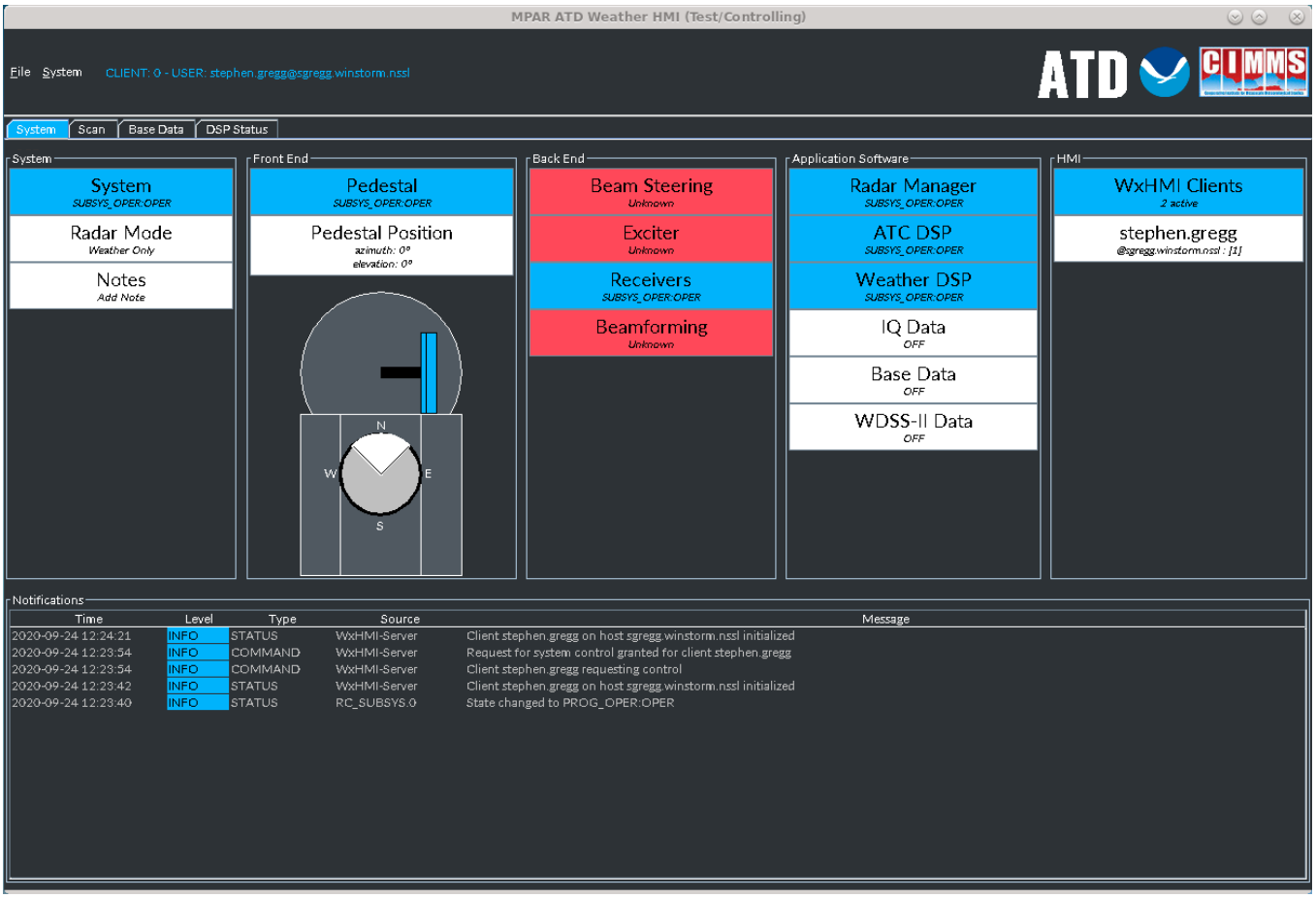

Figure 2.4.1. System panel of the Weather-HMI used to control and monitor the ATD.

Meteorological data collected with the Wx-HMI incorporates the following checks/calibrations:

- Waveform check: this check ensures that transmit/receive waveforms meet design requirements and will not damage the antenna. Waveforms that do not pass this check are not loaded into the exciter and cannot be used for data collections.
- Range calibration: this calibration determines range-adjustment parameters to place radar returns in their correct range location; it accounts for all system delays and processing that may affect the apparent range of targets. It is a function of the waveform.
- Absolute RCS calibration: this process determines the system reflectivity calibration constant (commonly referred to as "*SYSCAL*") to produce calibrated radar reflectivity values.
- Broadside calibration: this calibration determines the differential power and phase offsets between the H and V polarizations at broadside (on PRARs, these are commonly referred to as "Z_{DR} system bias" and "initial system Φ_{DP} bias").
- Beamsteering and cross-coupling bias calibration: this process determines magnitude corrections for both polarizations (H and V) as well as the differential power and phase offsets

between the copolar H and V polarizations as a function of electronic beamsteering angle relative to broadside. In addition, it determines the coefficients for the correction of cross-coupling effects. The corrections are derived from antenna copolar and cross-polar beam measurements and are applied in the real-time processing to calibrate estimates of reflectivity and polarimetric variables. However, the cross-coupling corrections are not currently used because the use of pulse-to-pulse phase coding effectively mitigates cross-coupling effects at lower elevation scans currently employed. Note that these bias corrections are relative to broadside and must be combined with broadside calibration constants to produce properly calibrated polarimetric data.

The following summarizes the basic processing steps used to obtain calibrated reflectivity and polarimetric variables on the ATD.

- Reflectivity:

  1. Estimate the mean signal power, $\hat{S}_{\mathrm{h}}$, in the H channel by computing the total mean power, $\hat{P}_{\mathrm{h}}$, and subtracting the noise power obtained with the Radial-by-Radial Noise (RBRN, Ivić et al. 2014) estimator, N_{h}. That is,

     $$\hat{S}_{\mathrm{h}} = \hat{P}_{\mathrm{h}} - N_{\mathrm{h}} .$$

  2. Compute a raw reflectivity estimate using the range, R, as adjusted by the waveform-dependent range-calibration constant, and compensating for atmospheric attenuation (*ATMOS*, typically 0.01 dB/km). That is,

     $$\hat{Z}_{\mathrm{raw}} = 10\log_{10}\hat{S}_{\mathrm{h}} + 20\log_{10} R + ATMOS * R .$$

  3. Compute the final reflectivity estimate by adding the broadside reflectivity calibration constant (*SYSCAL*) and compensating for the scan loss (*SL*), which is a function of beamsteering azimuth (ϕ) and elevation (90° - θ) angles (where ϕ and θ are spherical coordinates relative to the antenna face). That is,

     $$\hat{Z} = \hat{Z}_{\mathrm{raw}} + SYSCAL + SL(\phi,\theta) .$$

     Note that this calibration is conducted under the assumption that the cross-coupling effects are not appreciable in the estimates of signal powers in the H and V channels.

- Polarimetric Variables:

  1. Estimate the mean signal powers in the H and V channels, $\hat{S}_{\mathrm{h}}$ and $\hat{S}_{\mathrm{v}}$, by computing the total mean powers and subtracting the channel-specific noise powers.

  2. Estimate the cross-correlation at lag-0 [i.e., $\hat{R}_{\mathrm{hv}}(0)$] between the H and V channels.

  3. Compute the corrected power and cross-correlation estimates using the beamsteering and cross-coupling bias correction matrices, which are a function of radar variable (x) as well as beamsteering azimuth (ϕ) and elevation (90° - θ) angles. That is,

$$\begin{bmatrix} \tilde{S}_{\mathrm{h}}^{(x)} \\ \tilde{S}_{\mathrm{v}}^{(x)} \\ \tilde{R}_{\mathrm{hv}}^{(x)}(0) \end{bmatrix} = \begin{bmatrix} C_{11}(x,\phi,\theta) & C_{12}(x,\phi,\theta) & C_{13}(x,\phi,\theta) & C_{14}(x,\phi,\theta) \\ C_{21}(x,\phi,\theta) & C_{22}(x,\phi,\theta) & C_{23}(x,\phi,\theta) & C_{24}(x,\phi,\theta) \\ C_{31}(x,\phi,\theta) & C_{32}(x,\phi,\theta) & C_{33}(x,\phi,\theta) & C_{34}(x,\phi,\theta) \end{bmatrix} \begin{bmatrix} \hat{S}_{\mathrm{h}} \\ \hat{S}_{\mathrm{h}} \\ \hat{R}_{\mathrm{hv}}(0) \\ \hat{R}_{\mathrm{hv}}^{*}(0) \end{bmatrix}$$

4. Compute the polarimetric variables from the variable-specific corrected covariances using the conventional estimators. That is,

$$\hat{Z}_{\mathrm{DR,raw}} = 10\log_{10}\left[\frac{\tilde{S}_{\mathrm{h}}^{(Z_{DR})}}{\tilde{S}_{\mathrm{v}}^{(Z_{DR})}}\right],$$

$$\hat{\Phi}_{\mathrm{DP,raw}} = \arg\left[\tilde{R}_{\mathrm{hv}}^{(\Phi_{\mathrm{DP}})}(0)\right], \text{ and}$$

$$\left|\hat{\rho}_{\mathrm{hv}}\right| = \frac{\left|\tilde{R}_{\mathrm{hv}}^{(|\rho_{\mathrm{hv}}|)}(0)\right|}{\sqrt{\tilde{S}_{\mathrm{h}}^{(|\rho_{\mathrm{hv}}|)}\tilde{S}_{\mathrm{v}}^{(|\rho_{\mathrm{hv}}|)}}} \ .$$

5. For differential reflectivity and differential phase, subtract the corresponding biases computed via broadside calibration (denoted as "*SYS_ZDR"* for "Z_{DR} system bias" and "*SYS_PHIDP"* for the "initial system Φ_{DP} bias"). That is,

$$\hat{Z}_{\mathrm{DR}} = \hat{Z}_{\mathrm{DR,raw}} - SYS\_ZDR \ , \text{ and}$$

$$\hat{\Phi}_{\mathrm{DP}} = \hat{\Phi}_{\mathrm{DP,raw}} - SYS\_PHIDP \ .$$

Note that in the case whereby only copolar biases are corrected (and the cross-coupling biases are mitigated via phase coding), the beamsteering and cross-coupling bias correction matrices in step 3 are diagonal since only copolar pattern measurements are used for the computation of the corrections. If both co- and cross-polar patterns are used for correction computations (i.e., both the beamsteering and cross-coupling biases are corrected), the beamsteering and cross-coupling bias correction matrices have all non-zero elements. The bias measurement procedures are described in the next section.

3. ATD Polarimetric Calibration Procedures

Polarimetric calibration on the ATD consists of the four procedures defined in the previous section. These are: range calibration, RCS calibration, broadside calibration, and beamsteering and cross-coupling bias calibration. We utilize the Calibration Tower to conduct all calibration procedures. The first three procedures are performed with the ATD antenna pointing directly towards the FF probe (i.e., the radar beam is steered at broadside); these are described next.

In general, absolute RCS calibration requires a reference target with known RCS. For the ATD, this would naturally be the Calibration Tower. Unfortunately, we do not know the RCS of the Calibration Tower, so a one-time procedure was devised to estimate it. First, a baseline estimate of the broadside reflectivity calibration (*SYSCAL*) constant was derived by comparing simultaneous weather observations collected with the ATD and the KOUN radar. While KOUN was assumed to be properly calibrated, the

ATD used a *SYSCAL* constant of 0 dB. Because these radars have different beamwidths and used different scan strategies, the first step was to match the spatial sampling grids. To this end, the reflectivity field from the ATD was linearly interpolated into a polar grid matching the one used by KOUN, and both datasets were aligned in azimuth and range. The ATD baseline *SYSCAL* constant was obtained as the constant that, when added to the ATD reflectivity, minimized the root-mean-squared (rms) reflectivity differences between the ATD and KOUN fields. Next, the ATD antenna was mechanically pointed at the FF probe on the Calibration Tower, and the same waveform that was used to collect the weather data in the previous step was transmitted, looped back through the optical delay line (ODL), and re-transmitted over the air to the ATD. Received IQ samples were recorded and processed to obtain a range profile of signal powers from which the range gate with the maximum value was selected as the one corresponding to the Calibration Tower return. The baseline *SYSCAL* constant was then used to estimate the reflectivity of the Calibration Tower in the conventional way as described in the previous section. The result of this one-time process was an accurate estimate of the reflectivity of the Calibration Tower, which provides the required reference for the absolute RCS calibration.

The range and absolute RCS calibrations are performed as follows. First, the ATD antenna is mechanically pointed directly at the FF probe that is oriented in the horizontal polarization. Then, a pre-defined sequence of waveforms is transmitted from the ATD to the FF probe in rapid succession. Waveforms are received by the FF probe and are injected into the ODL, which increases the apparent range of the FF probe being measured by the ATD. Data from the ODL are re-transmitted to the ATD over the air and processed by the Wx DSP in the conventional way. Next, the FF probe is rotated into the vertical polarization, and the process is repeated for measurement of the same quantities in the vertical polarization. Then, the reflectivity of the Calibration Tower is used to derive waveform-specific *SYSCAL* constants for all ATD waveforms. That is, regardless of the waveform used, the ATD should measure the same reflectivity for the Calibration Tower. The same data set is used for waveform-dependent range calibration. Given that the ATD base-data range sampling is 225 m, a parabolic fit (with the peak point and its two adjacent neighbors in the range profile) is used to improve the accuracy of the range calibration. The range of the peak in the parabolic fit is extracted and used to calculate a waveform-dependent range offset. That is, since the actual location of the FF probe and the configuration of the ODL are known, the actual range to the ATD can be calculated. Then, the difference between the apparent and actual ranges is computed and is used to compute a range calibration adjustment. An example reflectivity profile, with the interpolated parabolic function, is shown in Figure 3.1.

The broadside bias calibration produces waveform-dependent Z_{DR} bias and initial system Φ_{DP} bias values, as follows. The data collection procedure is identical to the previous one; i.e., the ATD antenna is mechanically pointed at the FF probe and a pre-defined sequence of waveforms is measured, first with the FF probe in the horizontal orientation and then in the vertical. These data are processed by the ATD receiver as in the previous procedure. Then, the difference between the peaks in the range-weighting functions of horizontal and vertical polarization returns is computed. This differential reflectivity between H and V is the system Z_{DR} bias (i.e., *SYS_ZDR*). The phases of the H and V signals are also computed at the peak of the range-weighting function. Their difference is calculated to produce the initial system Φ_{DP} bias values

(i.e., *SYS_PHIDP*). The outputs of this calibration (for a set of 62 pre-defined waveforms) are shown in Figure 3.2.

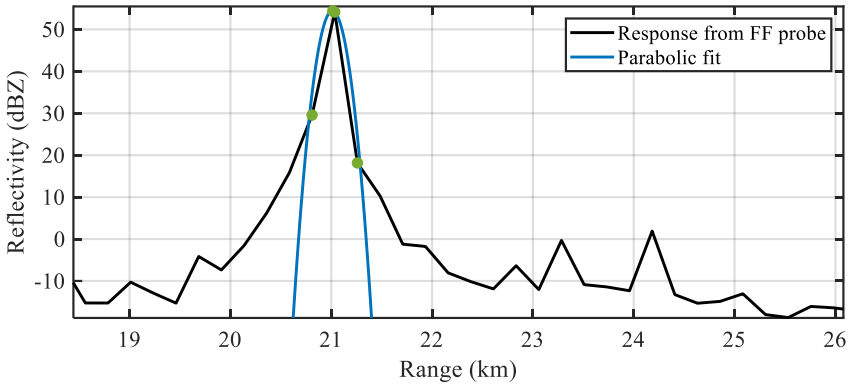

Figure 3.1. Example reflectivity profile from the range and reflectivity calibration sequence. The solid black line shows the reflectivity produced by the Wx DSP, and the blue line shows the parabolic fit from which the range calibration adjustment is derived.

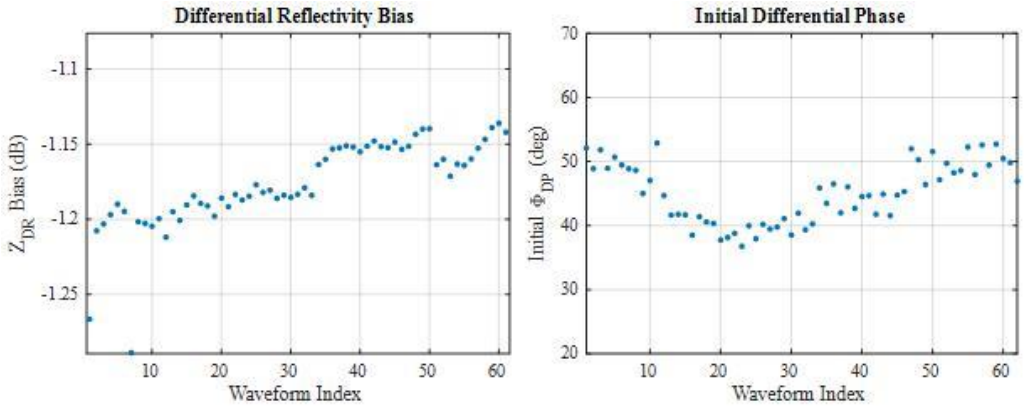

Figure 3.2. Example broadside bias calibration sequence, which produces system differential reflectivity and initial differential phase as a function of the weather-scan waveforms.

In the case of beamsteering and cross-coupling bias calibration, the fourth procedure, it is necessary to characterize the beams (at and around beam peaks) for multiple electronic steering angles due to the existence of scan-dependent copolar and cross-polar patterns. On a typical weather scan, the ATD electronically scans a sector that spans ±45° in azimuth and 0-20° in elevation while the antenna is stationary. This poses a requirement that beams be characterized for electronic steering angles in this domain. Accordingly, the calibration procedure currently performs beam measurements at electronic beamsteering angles that span azimuths of ±45° in 3° steps and elevations 0-20° in 2° steps for a total of 31×11=341 beam measurements. To measure the steering dependent biases for a given electronic angle, we employ a multi-step calibration procedure. At each measurement point, the antenna is mechanically placed into position so that when the beam is electronically steered in the direction to be measured, it points towards the FF probe location. To achieve this, we developed an algorithm that calculates the antenna mechanical position (i.e., azimuth and elevation) given the measured beamsteering direction relative to the antenna face using the known location of the FF probe. For each beam measurement, a small scan is executed to capture

the beam centers and a neighborhood around them. That is, the area around the expected beam peak is scanned electronically using a so-called box scan and alternating between transmit and receive beams to create copolar and cross-polar quasi-pattern data. This process is executed for the horizontal and vertical FF probe polarizations. It is entirely automated and is graphically depicted in Figure 3.3. The data from each box scan are processed to produce a set of beam measurements for a given electronic beamsteering angle. The resulting beam measurements are finally fitted with high-order polynomials in azimuth and elevation to produce matrices of calibration values on an electronic beamsteering grid with 0.25° steps in both azimuth and elevation. In its current version, the beamsteering and cross-coupling bias calibration procedure takes ~4.5 hours to execute.

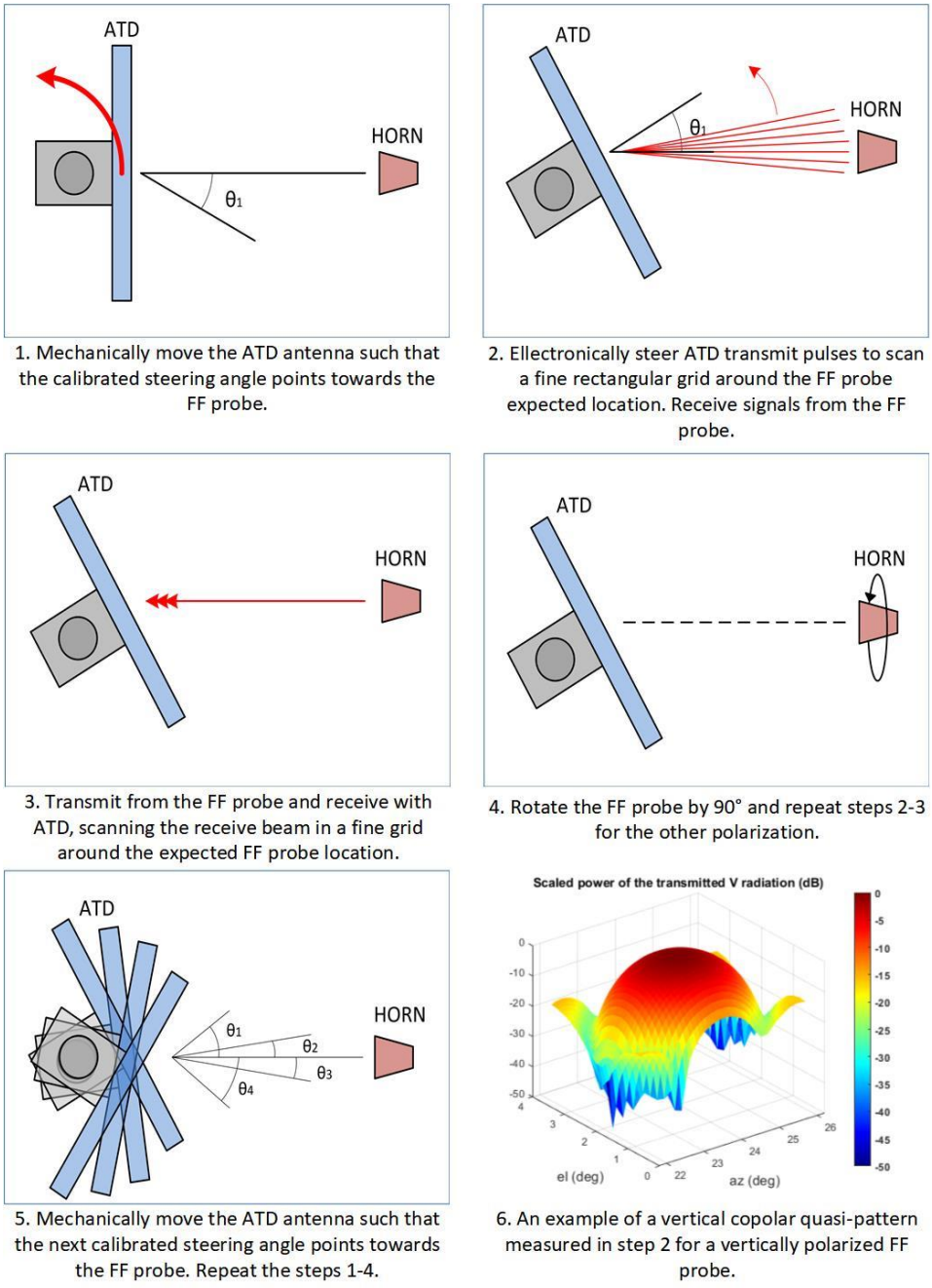

Figure 3.3. Depiction of beam characterization procedure.

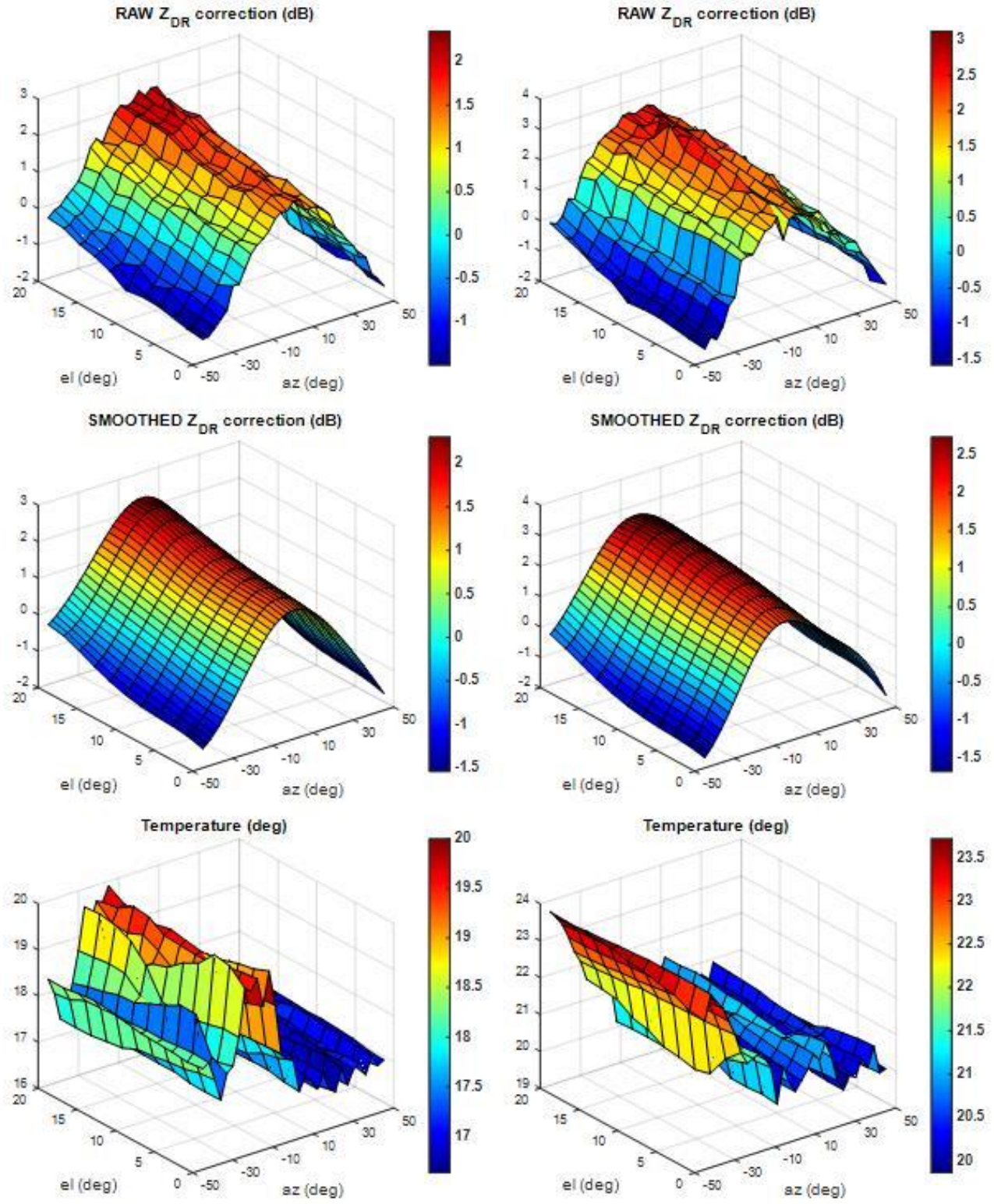

Figure 3.4. 3-D depiction of element C_{22} in the Z_{DR} correction matrix derived from calibration data collections on 7/23/20 (left column), and 10/1/20 (right column). The top and middle panels show raw and smoothed calibration data, respectively. Bottom panels show average array temperature (in ºC) derived from 7 sensors located throughout the ATD antenna.

We use data collected with the process previously described to derive beamsteering and cross-coupling bias corrections. The derivation procedure is quite complex since it involves the bias model based on antenna patterns (Ivić 2018), attention to details described in Ivić 2018a, as well as corrections due to the ATD antenna tilt relative to the ground. Examples of Z_{DR} estimate corrections (for beamsteering biases only) computed from two calibration runs are given in Figure 3.4. Note that similar corrections are also computed for reflectivity and differential phase but are not shown here. Figure 3.4 shows differential reflectivity corrections along with the average array temperatures for each collection point. Note that the raw correction results are noisy due to multiple practical effects (e.g., multipath and temperature variations). For this reason, the raw results are smoothed to improve accuracy. Furthermore, investigations conducted so far indicate that the results depend strongly on the array temperature fluctuations during the calibration procedure. The resulting differences from the two collections that lead to Z_{DR} biases larger than the desired 0.1 dB are attributed to temperature effects. The effects of temperature fluctuations are demonstrated in Figure 3.5 where the *Z* beamsteering correction results are shown for a 0° elevation since these are the most susceptible to temperature drifts. A comparison between the *Z* beamsteering biases computed from the two calibration runs reveals significant asymmetries between the left and right halves of the curves. The current hypothesis is that the asymmetries are caused by the array temperature variations since the near-field measurements indicate that these should be approximately symmetric (see Figure 2.3.1). The relationship between the measurement results and the array temperature is still an open question that is currently being investigated.

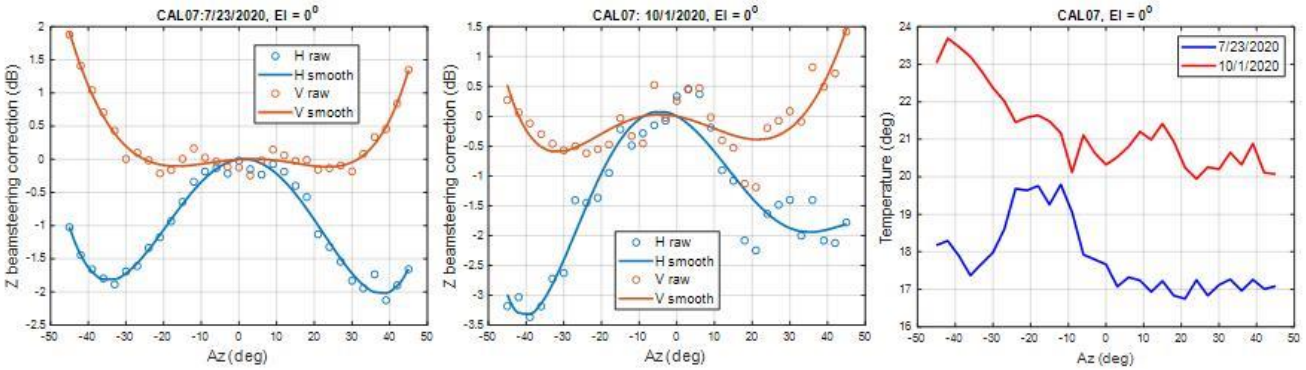

Figure 3.5. Reflectivity beamsteering bias correction results from 7/23/2020 (left panel), and 10/1/2020 (middle panel), as well as associated array temperatures during both collections (right panel).

4. Application of Beamsteering Bias Calibration

The beamsteering bias calibration was tested on data sets collected consecutively on August 22, 2019, via twelve scans, which were collected at antenna mechanical positions gradually shifted by 10° in azimuth and at a constant elevation of 0.5°. At every mechanical position, a 90° sector (±45° relative to the antenna broadside) was scanned. This created sector scans that are overlapped in azimuth. Because the time difference between consecutive scans is ~1 min, we can assume little-to-no storm evolution from one scan to the next. The overlapping parts of these scans can be used to assess the differences in estimated polarimetric variables from collocated volumes illuminated using different electronic steering angles. The differences were analyzed when no corrections were applied for the effects of beamsteering and after

applying the copolar polarimetric corrections described in the previous section (this process is referred to as a self-consistency check). The ATD data presented in this section was not collected using pulse-to-pulse phase coding. Nonetheless, because the beams were steered only 0.5° away from the horizontal principal plane, we assume that the cross-coupling effects were small enough and can be neglected for this test.

4.1. Self-Consistency Improvement

The results before and after beamsteering bias calibration are presented in Figure 4.1.1 and Figure 4.1.2. Visual comparison of overlapping areas reveals differences in Z_{DR} and Φ_{DP} between estimates from different scans in Figure 4.1.1. These differences are induced by the system as indicated by the near-field measurements (Figure 2.3.1). The system-induced bias effects are the most visible towards the edges of each scan sector. After calibrating, the differences are visibly reduced as demonstrated in Figure 4.1.2. Further, the differences at each beamsteering position were averaged in range and are shown in Figure 4.1.3 along with differences predicted by the calibration procedure.

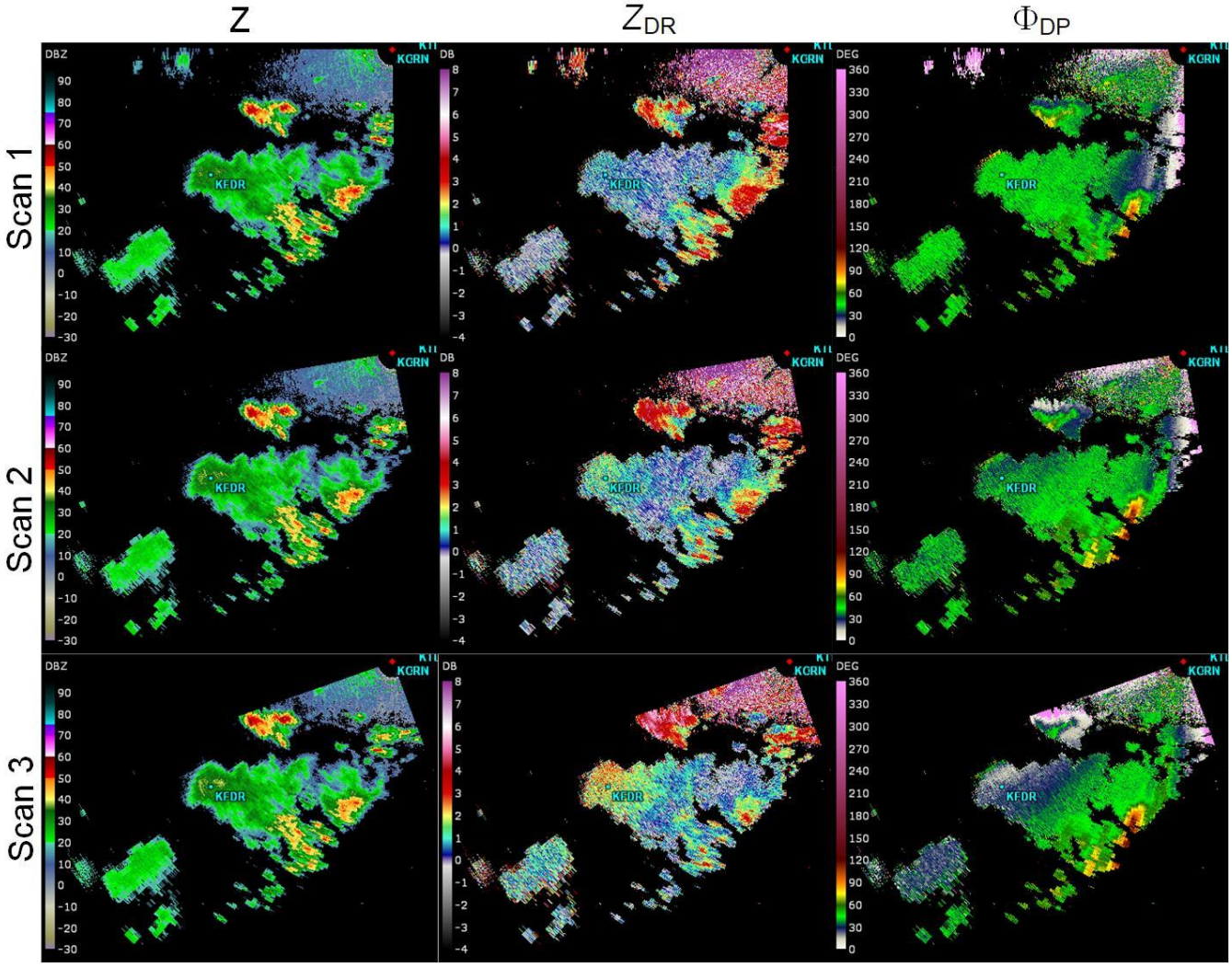

Figure 4.1.1. Raw uncalibrated estimates of reflectivity (left column) differential reflectivity (center column) and differential phase (right column) for three consecutive sector scans with mechanical antenna shifts of 10° in azimuth between scans.

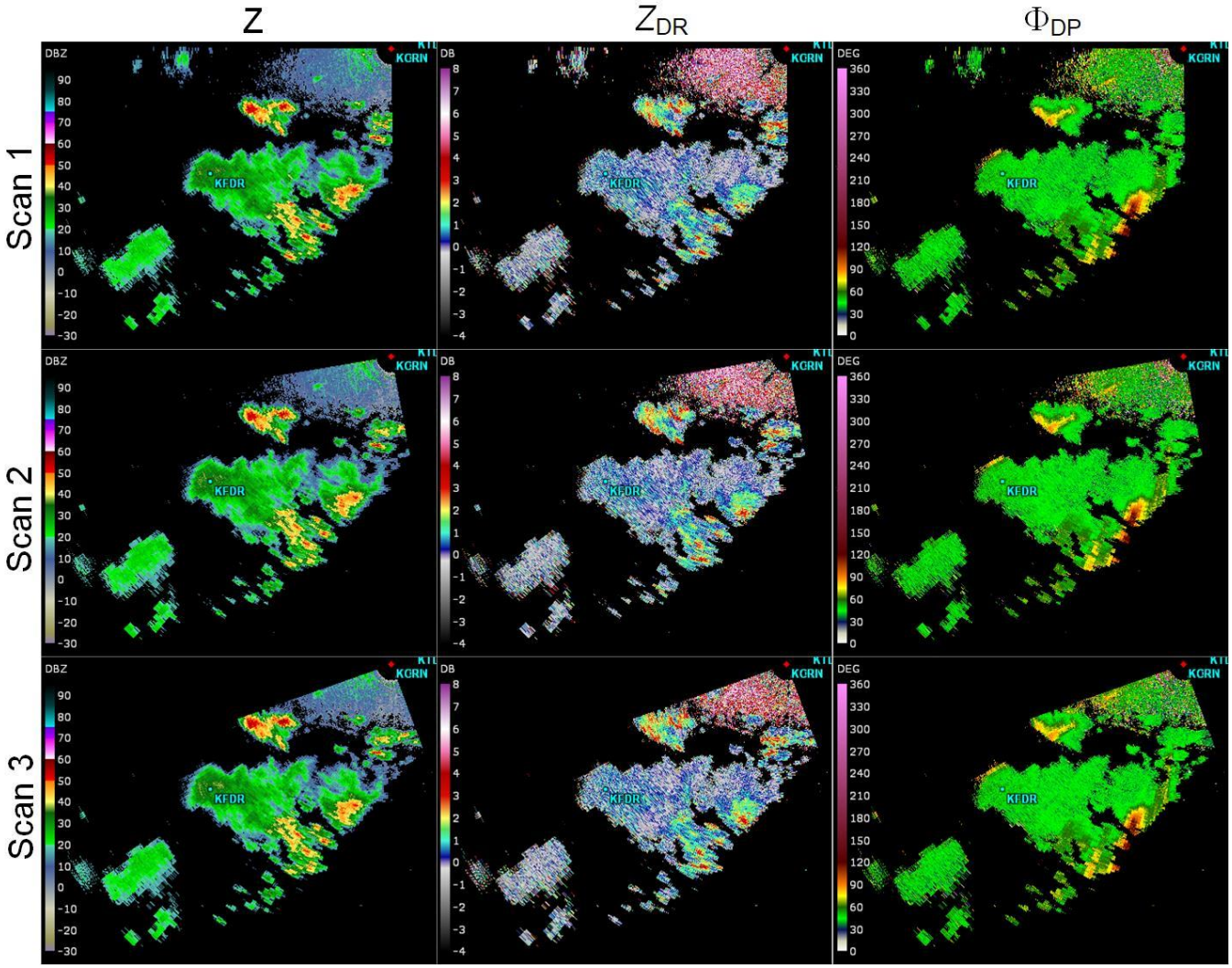

Figure 4.1.2. Same as Figure 4.1.1. after beamsteering bias calibration.

The range-averaged differences of corrected (calibrated) and uncorrected (uncalibrated) *Z* estimates are rather noisy; and they both show a span of biases of ~±1 dB (dashed and solid black lines in the upper left panel of Figure 4.1.3), which is similar to the one predicted by the calibration measurements (solid grey line in the upper left panel of Figure 4.1.3). Because, the *Z* color scales in Figure 4.1.1 and Figure 4.1.2 are in steps larger than 1 dB, the *Z* biases are not noticeable in the leftmost panels of Figure 4.1.1. In the case of Z_{DR} (upper right panel of Figure 4.1.3), the agreement between the bias predicted by the calibration process and those measured from uncorrected Z_{DR} estimates is clearly visible for azimuths within ±30° but degrades outside this range. This is also corroborated by the differences using corrected Z_{DR} estimates (solid black line in the upper right panel) as the fluctuations around zero become larger outside the ±30° interval. The results for Φ_{DP} (lower left panel), also exhibit a good matching between differences measured using uncalibrated estimates and calibration predictions. Accordingly, the differences derived from calibrated estimates exhibit relatively small fluctuations around zero over most of the measured interval with the distinction of several significant spikes that are attributed to estimation artifacts. In a broader statistical sense, the benefits of Z_{DR} calibration are demonstrated by the histograms of Z_{DR} differences before and after

calibration (the lower right panel in Figure 4.1.3). The histogram before calibration is asymmetric and indicates a large dispersion of results while the histogram after calibration becomes much more symmetric and indicates significantly less dispersion of differences with a mean value at ~0 dB. This is a clear indication of largely reduced system beamsteering biases after the application of corrections derived from the calibration process described in the previous section.

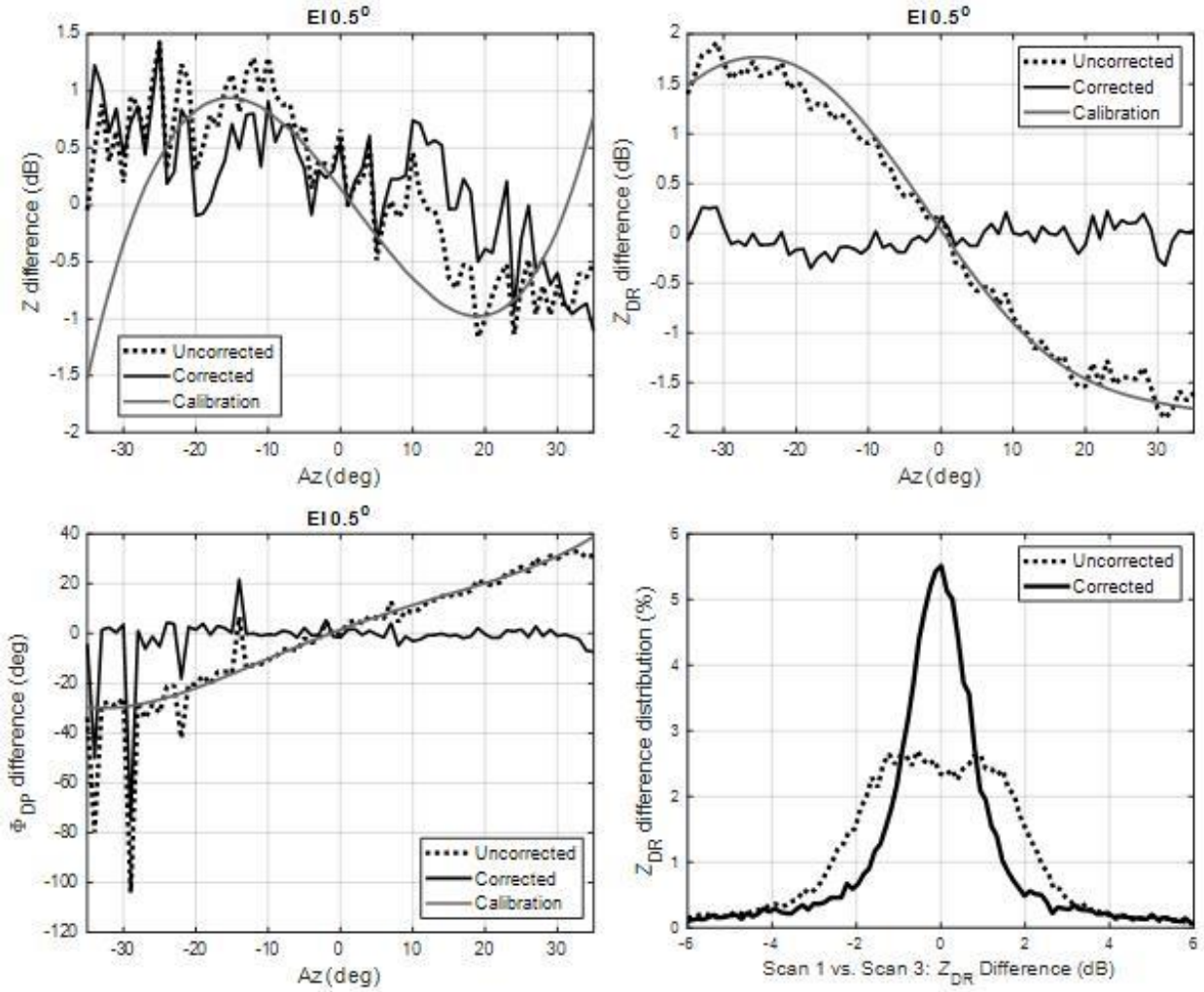

Figure 4.1.3. Range-averaged system-induced differences between estimates from collocated volumes illuminated during scans 1 and 3 (upper and lower left panels) as well as histograms of Z_{DR} differences before and after calibration (lower right panel). The differences predicted by the calibration procedure are shown in grey for reference.

4.2. Comparison with Other Radars

In this section, we compare ATD data to data from the KCRI radar, which is operated and maintained by the Radar Operations Center and is collocated with the ATD.

ATD data used in the analysis herein were collected during the May 1st, 2019 severe-weather event using pulse-to-pulse phase coding. For this data collection, the array was mechanically positioned with the boresight direction pointed at 192° in azimuth and 0° in elevation, and the beam was electronically steered ±45° in azimuth at a constant elevation of 0.5°. At each beam position, the ATD used a triple-PRF dwell

with 12 samples at T_1 = 3 ms, 20 samples at T_2 = 1 ms, and 15 samples at T_3 = 1.5 ms. Pulse compression with a pulse length of 38 μs was used to increase sensitivity. It was followed by a 1.8 μs fill pulse to collect data at close ranges blanked by the long pulse. Receiver range-time samples were produced at a rate of 4 MHz, which resulted in a range sampling interval of 37.5 m. Range-time processing was set to incoherently average samples from 6 consecutive range gates, which resulted in a range sampling spacing for the radar variables of 225 m. The data were collected with the ATD radar at 19:57:44 Z, and both level-I and level-II data were recorded for posterior analysis. The KCRI radar was following the operational VCP 212, which commands the antenna to rotate at 21.5° s^{-1} to collect surveillance scan (CS) data and at 17.1° s^{-1} to collect Doppler scan (CD) data, both at the 0.5° elevation angle. For this elevation, the dwell definitions for the CS and CD scans are 15 samples at T_{CS} = 3 ms and 64 samples at T_{CD} = 1 ms, respectively. Surveillance scan data for the 0.5° elevation were collected with the KCRI radar at 19:57:43 Z, and time-series IQ data for the same azimuthal sector as the one scanned by the ATD system were extracted for off-line processing. Note that the KCRI radar has better sensitivity and angular resolution than the proof-of-concept ATD radar, and therefore some differences in estimated fields are expected.

Fields of radar-variable estimates resulting from processing the data from these scans are presented in Figure 4.2.1. Panels are organized as follows: the top row corresponds to uncalibrated ATD data, the middle row corresponds to ATD data corrected with calibration products as described in section 3, and the bottom row corresponds to KCRI data; the columns from left to right show fields of Z_h, Z_{DR}, Φ_{DP}, and $|\rho_{hv}|$. Herein, only corrections for copolar biases are applied since our research to date indicates that pulse-to-pulse phase coding sufficiently mitigates the cross-coupling effects at the beamsteering directions used in this test. Note that for comparison completeness, we also include the results for the copolar correlation coefficient ($|\rho_{hv}|$) estimates even though no corrections are applied to this product (i.e., there is no difference between the upper and middle panels in the fourth column of Figure 4.2.1). This is because the bias in $|\rho_{hv}|$ estimates is exacerbated by the cross-coupling effects but is unaffected by the variations in copolar patterns that cause the beamsteering bias.

Let us first conduct a qualitative comparison of calibrated ATD and KCRI fields. A comparison of corresponding fields shows good agreement between estimates; i.e., similar features with approximately the same values and in approximately the same locations. Fields of calibrated ATD Z_{DR} and KCRI Z_{DR} present similar qualitative features. Regions with large drops (high Z_{DR} ~ 3 dB or higher) approximately coincide in location and size, as well as in the estimated values. Comparing the sector edges of the uncalibrated and calibrated ATD Z_{DR} estimates, it is clear that the calibration reduced the large copolar beamsteering biases. For both radars, the differential phase is unwrapped so that the initial system differential phase is set to about 60° (blue in the figure). This occurs at locations where propagation effects are small, such as close to the radar, and may extend in range if precipitation is light. The radially oriented "streak increase" of Φ_{DP} for azimuths between 160° and 180° is caused by heavy rain (possibly containing ice cores) in the discrete convective cell to the southeast of the ATD (white circle in the Z_h panel) as the radar beam propagates through it. After correction, the data from both radars show an increase of about 40° (light green category representing 100°) from close to the radar to about 100 km. The convective cell contributes about 30° over a 6 km distance. Ryzhkov and Zrnić (2019, p. 172) refer to this phenomenon as a "hot spot." A similar elongated radial feature at an azimuth of about 190° is also caused by heavy

precipitation as the radar beam propagates through a convective cell along this radial. Both radars observe approximately a 100° increase in Φ_{DP}, and the shapes of the contours are in good agreement (because of lower detectability, the ATD misses some data at the farthest ranges). A good overall agreement of the ATD and KCRI Φ_{DP} and Z_h fields suggests that rainfall measurements based on the attenuation method—which relies on Z and changes in Φ_{DP} (Ryzhkov and Zrnić 2019)—or specific differential phase would be better suited to PPARs compared to alternatives that require calibrated Z_{DR}. All fields of $|\rho_{hv}|$ present similar features given that beamsteering biases have no impact on the quality of $|\rho_{hv}|$. In particular, the region indicated with blue rectangles in $|\rho_{hv}|$ panels contains a mixture of estimates, some of which are relatively low ($|\rho_{hv}| \sim 0.85$). Further, the strong reflectivity gradient ($Z_h > 60$ dBZ), the low-to-moderate Z_{DR} values (~0–1 dB) mixed with higher values (>1 dB), and the "streak increase" of Φ_{DP} (indicating high Φ_{DP} gradient) in the marked region, indicate a likely presence of a hail core (in the upper right corner of the rectangle) as well as hail-rain mixtures.

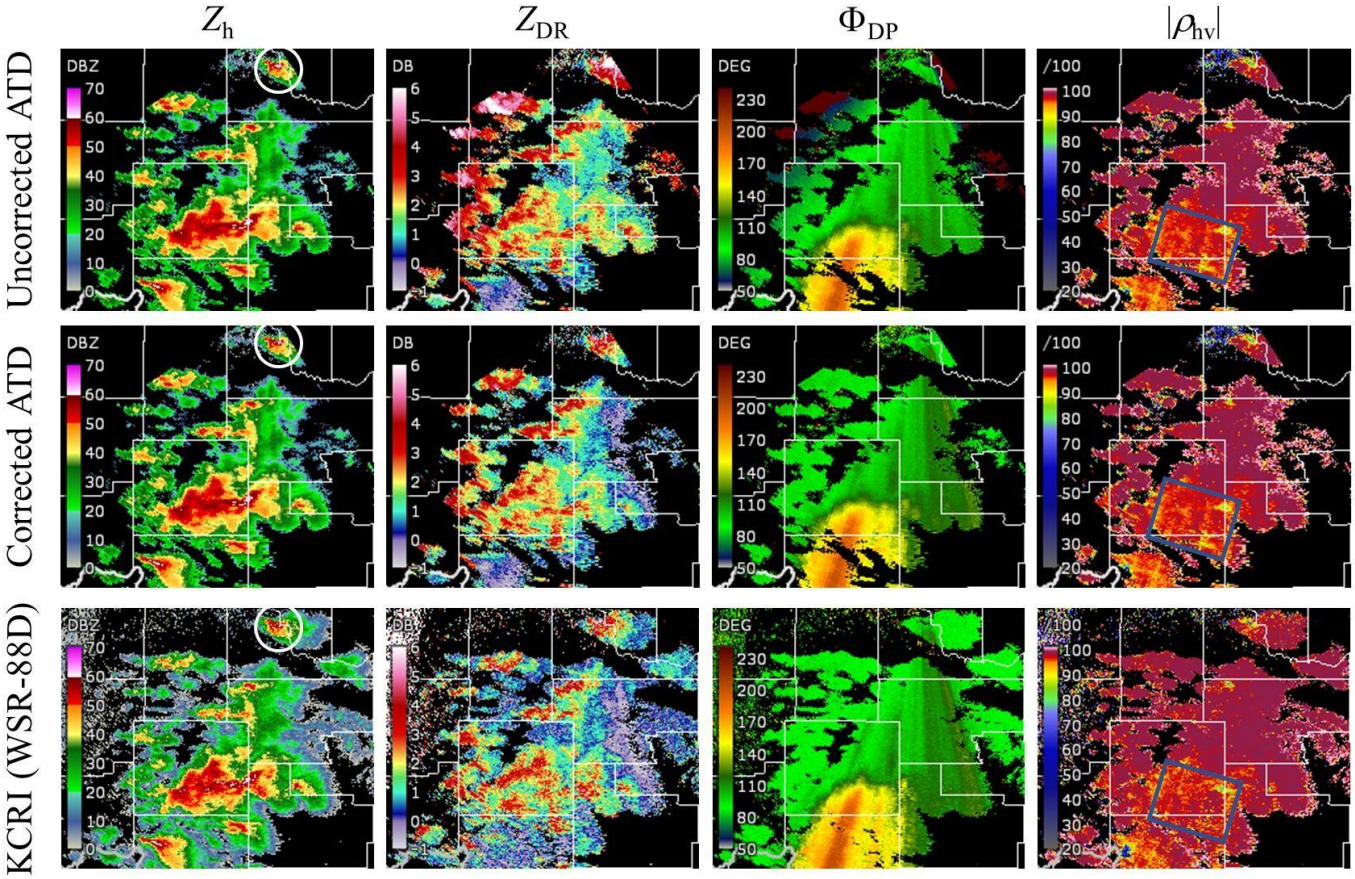

Figure 4.2.1. ATD reflectivity and polarimetric variable fields on 1 May 2019, (top row) without and (middle row) with beamsteering bias calibration. The bottom row is concurrent data from the collocated KCRI. The ATD and KCRI data were collected at approximately the same time (19:57:43 Z) and at an elevation angle of 0.5°. The maximum range in these images is ~125 km.

Next, we conduct a quantitative evaluation of the quality of estimates obtained with the ATD with respect to KCRI. Differences between these radar systems such as radar frequency (both are S-band radars), sensitivity, beamwidth and sidelobe levels, and antenna height with respect to the ground were neglected

for this comparison. The bivariate density maps in Figure 4.2.2 are computed from these fields of estimates using an SNR threshold of 10 dB; they serve to illustrate the correlation between estimates derived from the two radar systems. These density maps are normalized to approximate a probability density function. That is, the value at each bin is computed as the number of observations that fall in that bin divided by the total number of observations and multiplied by the scaling factor (i.e., the area of a bin divided by the area covered by all bins). The Pearson correlation coefficient (r) between the estimates is indicated in each sub-figure title. It indicates a significant correlation (i.e., $r > 0.9$) for Z_h and Φ_{DP} estimates, a considerable correlation for Z_{DR} estimates, and a moderate correlation for $|\rho_{hv}|$ estimates.

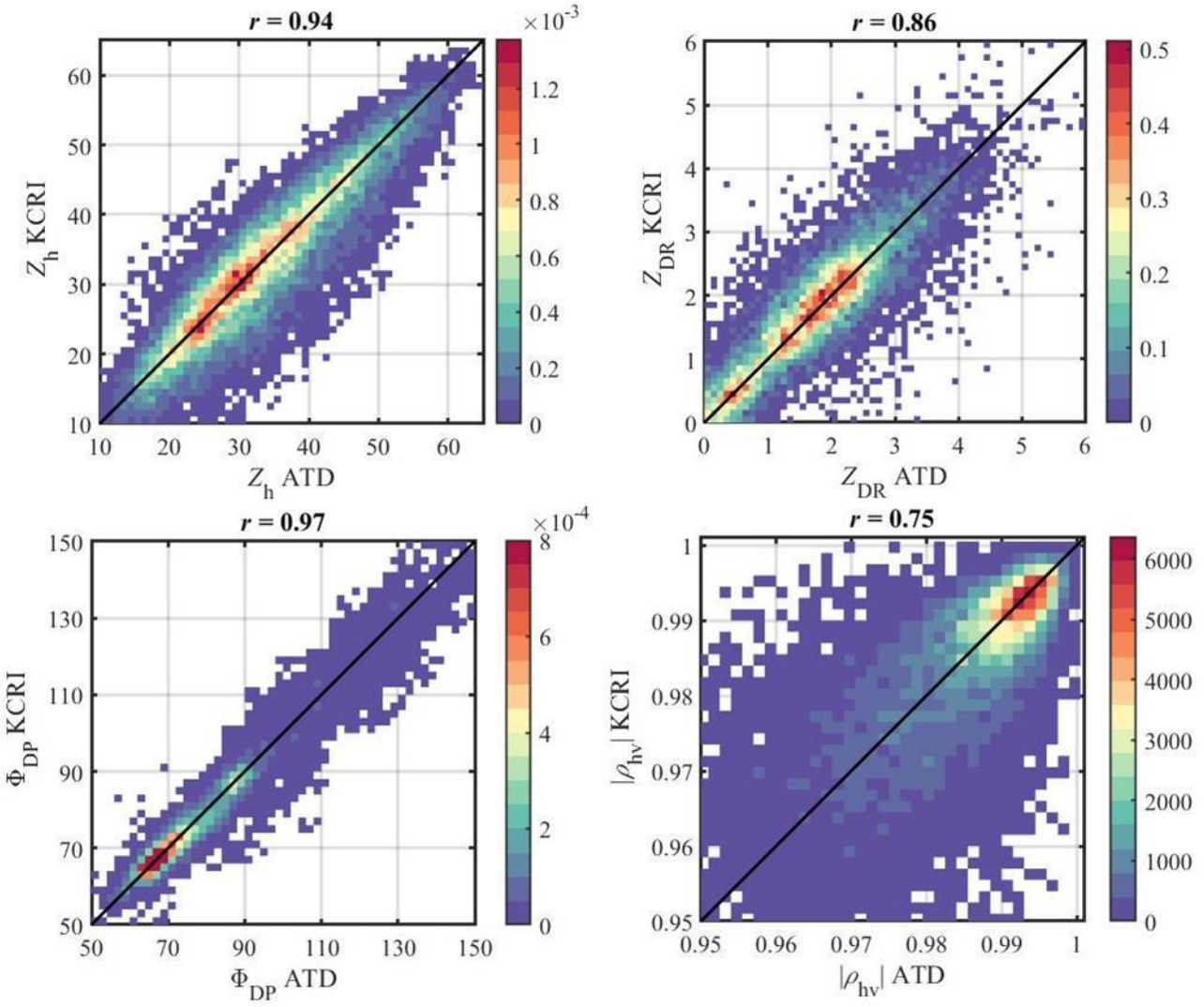

Figure 4.2.2. Bivariate density maps computed from fields of radar-variables estimates from the ATD and KCRI scans in Figure 4.2.1 for Z_h (upper left panel), Z_{DR} (upper right panel), Φ_{DP} (lower left panel), and $|\rho_{hv}|$ (lower right panel). The Pearson correlation coefficient (r) between the estimates is indicated in each sub-figure title.

Significant correlations between corresponding Z_h and Φ_{DP} estimates are very promising; they validate the effectiveness of the calibration procedure described in Section 3. Density maps for those variables are narrow and symmetric about the $x = y$ line. Correlation between Z_{DR} estimates is considerable ($r > 0.85$),

and the bivariate density map is well aligned with the $x = y$ line. There is a larger spread of $|\rho_{hv}|$ estimates about the $x = y$ line but estimates from both systems appear to be well concentrated in the 0.98–0.99 range. This could be due to system differences (e.g., beamwidth); although the same signal processing algorithms (e.g., noise estimator, clutter filtering, etc.) were used to process both datasets, there are several differences between radar systems. Further, the performance of $|\rho_{hv}|$ lag-0 estimator (used herein) depends strongly on SNR since the standard deviation of $|\rho_{hv}|$ estimates increases at a rate several times larger than Z_{DR} and Φ_{DP} estimates as SNR declines. Thus, it is likely that the increase in the spread of values in the bivariate $|\rho_{hv}|$ map is a consequence of the larger fluctuations in $|\rho_{hv}|$ estimates from both radars that is further exacerbated by the fact that, for a given location, the SNR in the ATD data is considerably lower than in the KCRI data. Nonetheless, the spread of values in the lower right panel of Figure 4.2.2 appears symmetric around the $x = y$ line indicating good agreement among the mean $|\rho_{hv}|$ estimates from both radars.

We find these preliminary results very encouraging and consistent with results from the self-consistency check as both tests demonstrate visible and measurable reduction of the beamsteering bias effects after calibration. In addition, the results in this section include a comparison between the copolar correlation fields from the ATD and the parabolic-reflector KCRI radar, corroborating the validity of this ATD product for which no corrections were applied in this test.

5. Summary and Conclusions

The ATD is being used as a testbed for investigating the use of PPAR for weather observations. To support research towards operationally feasible PPAR calibration techniques, a Calibration Tower with the associated infrastructure was installed near the ATD site. This calibration infrastructure supports both system health checks and calibration measurements. The latter is particularly important for weather observations because scan dependent system-induced biases are inherent in PPAR systems. These biases are measured through appropriate calibration procedures so that proper corrections can be derived and applied in real-time processing while collecting weather data.

In this report, we described the four calibration procedures that are aimed at improving the accuracy of weather observations on PPARs. The first is the range calibration procedure, which ensures accurate placement of radar echoes in range. The second procedure provides reflectivity calibration, and the third one measures the system-induced biases in differential reflectivity and phase estimates when the beam is directed at broadside. Note that these three calibration procedures (or variants thereof) are not exclusive to PPARs but are required for all polarimetric radars. The last calibration procedure is the beamsteering and cross-coupling bias calibration. This procedure produces corrections for the system-induced biases from electronic beamsteering as well as cross coupling, which are inherent in PPARs (but not in PRARs). This procedure is the most involved of all four calibration procedures and its appropriate design and implementation are the main reasons that calibration of PPARs remains a challenge. Currently, the beamsteering and cross-coupling bias calibration procedure execution time is ~4.5 hours due to the required large number of measurement points. However, it should be noted that the current ATD standard mode of operation is to electronically scan a sector of space while the antenna is stationary. Such mode of operation requires correction of scan-dependent system-biases for a large number of electronic steering angles that results in the lengthy calibration procedure. Furthermore, a significant number of steering directions are

located far enough from the principal planes where cross-polar patterns are significant, which adds to the calibration difficulty. This mode of operation is envisioned for an operational PPAR with four stationary antennas oriented perpendicular to each other with every antenna covering a distinct sector assigned to it. It is unlikely, though, that such architecture will be affordable to NOAA. Hence, a more feasible operational architecture is a PPAR with one antenna mounted on a rotating pedestal (i.e., rotating phased array radar or RPAR). In this regard, an alternative mode of ATD operation (in support of RPAR) is the one whereby the antenna rotates mechanically and the beam is steered electronically only in elevation. With such an approach, only beamsteering biases along the vertical principal plane need to be corrected, which significantly simplifies the beamsteering and cross-coupling bias calibration. However, to achieve the desired increase in the volumetric update times with RPAR, advanced techniques that require simultaneous transmission and reception of multiple beams must be employed (in this regard, the RPAR option and its aspects are a part of our research efforts as well). The multiple RPAR beams may scan a limited number of locations away from the vertical principal plane but that number would be significantly smaller than the full electronic steering region (±45º in azimuth and 0-20º in elevation). As a result, the beamsteering and cross-coupling bias calibration could be significantly simpler. Regardless of which PPAR architecture is chosen for the operational application, the results of our research with the ATD will be applicable.

The application of the polarimetric calibration procedures was demonstrated on weather observations with the ATD. Because the beamsteering and cross-coupling bias calibration procedure takes several hours, and the system temperature drifts appreciably during this period, the results exhibit temperature dependencies leading to significant impacts on the accuracy of the calibration. This suggests potential limitations of the antenna thermal-management approach, which on the ATD is based on air cooling. The temperature drifts measured in the ATD may be mitigated in future designs by adopting a liquid-cooling thermal management approach; it is likely that this approach would improve the system temperature stability although it is uncertain by what margin. Nonetheless, the calibrated ATD weather data exhibited tangible improvements compared to the uncalibrated data. This was demonstrated, by comparing ATD data sets collected at distinct antenna mechanical positions but scanning collocated volumes of space filled with hydrometeors. As a result of applying beamsteering-bias corrections, differences between the differential reflectivity and differential phase estimates from collocated volumes that are illuminated using distinct electronic steering angles were drastically reduced. This was verified by visual inspection whereby clearly identifiable artifacts of beamsteering biases were reduced through polarimetric calibration to the point of being inconspicuous. These improvements were further corroborated at each beamsteering position. To this effect, we compared differences derived from weather observations before calibration (and averaged in range for accuracy and consistency) with the corresponding differences predicted by the beamsteering and cross-coupling bias calibration. This comparison reinforced our qualitative analyses by showing reasonable agreement between the two computed differences. At the same time, the differences derived from the calibrated weather data exhibited fluctuations around zero, which is expected when the weather data are not affected by the beamsteering and cross-coupling effects. In summary, the statistical comparison between weather-derived beamsteering biases before and after polarimetric calibration clearly indicated that the biases were significantly reduced after applying proper corrections. Next, the fields of polarimetric variables produced by ATD were compared to those from the collocated KCRI radar. This comparison further

corroborated the findings from the previous analyses and demonstrated the effectiveness of the polarimetric calibration procedures as well as the benefits of applying appropriate corrections in our real-time signal processor.

Although we currently do not have sufficient data to precisely assess the accuracy of calibrated ATD products, we conjecture that it is unlikely that the biases in differential reflectivity required by the NWS were achieved at all beamsteering directions in these preliminary measurements. Such assessment will be done via self-consistency checks using a larger pool of weather data so that the beamsteering bias at each steering angle can be estimated reliably (e.g., see Figure 4.1.3). We plan to further evaluate the ATD data accuracy by conducting comparisons with the collocated WSR-88D radars. Another approach for data-quality assessment that is likely to appeal to the meteorological community is to generate Level III products from the ATD base data. These products could be evaluated via a self-consistency check as well by comparison to their WSR-88D counterparts. In light of this, our future investigations will be directed towards developing procedures and tools for evaluating the robustness and quality of the ATD polarimetric calibration.

In our preliminary assessment, the system temperature instabilities are a major obstacle to achieving our projected polarimetric data-quality goals. This is because the antenna system exhibits significant temperature fluctuations during the execution of the beamsteering and cross-coupling bias calibration procedure. As a result, the system parameters that are being measured change while the calibration procedure is executed, thus negatively affecting the results. Consequently, we will focus our future efforts towards researching the relations between the array temperature and the calibration results, with the ultimate goal to mitigate any system temperature dependencies. This may result in temperature-dependent corrections if we can confirm that the antenna characteristics are a well-defined function of temperature. If this approach fails, achieving the desired accuracies of differential reflectivity and/or reflectivity estimates may be unattainable with the ATD. Another effect adversely affecting the repeatability and accuracy of calibration measurements is multipath interference (i.e., a phenomenon whereby a wave from a source travels to a detector via two or more paths and the two or more components of the wave interfere constructively or destructively). We speculate, however, that the multipath interference effects may be effectively mitigated via smoothing of the noisy beamsteering and cross-coupling bias measurements.

After the dependency of calibration measurements with temperature has been established, we plan to focus on other important questions such as the stability and robustness of the calibration process. The former will help us determine the frequency of calibration execution while the latter will aid in identifying modifications to the current procedure or perhaps different polarimetric calibration approaches.

Concerning the operational feasibility of the polarimetric calibration presented here, it is possible that future operational PPARs will not have calibration towers from which the polarimetric-calibration measurements described in this report can be obtained. To address this, we are collaborating with a team of engineers at the Advanced Radar Research Center (ARRC) who are investigating the use of Unmanned Aircraft Systems (UAS) for in-situ antenna characterization, radome inspection, and radar calibration.

Finally, we find that the quality of the calibrated ATD weather products at lower elevations is sufficient for qualitative data interpretation. This was corroborated by two experts, Dr. Alexander Ryzhkov and Dr.

Dušan Zrnić, and suggests a promising outlook for our research efforts on the use of PPARs for weather surveillance.

References

Balakrishnan N., and D. S. Zrnić, 1990: Use of Polarization to Characterize Precipitation and Discriminate Large Hail. *J. Atmos. Sci., 47,* 1525–1540. Available at doi: http://dx.doi.org/10.1175/1520-0469(1990)047<1525:UOPTCP>2.0.CO;2

Conway, M. D., D. Du Russel, A. Morris, and C. Parry, 2018: Multifunction phased array radar advanced technology demonstrator nearfield test results. *Proc. of the IEEE*. Available at doi: https://doi.org/10.1109/RADAR.2018.8378771

Herd, J. S., S. M. Duffy, and H. Steyskal, 2005: Design considerations and results for an overlapped subarray radar antenna". *2005 IEEE Aerospace Conference*, 1087–1092. Available at doi: 10.1109/AERO.2005.1559399

Heinselman, P. M., and S. M. Torres, 2011: High-Temporal-Resolution Capabilities of the National Weather Radar Testbed Phased-Array Radar. *J. Appl. Meteor. Climatol., 50(3),* pp. 579-593. Available at doi: http://dx.doi.org/10.1175/2010JAMC2588.1

Ivić, I. R., C, Curtis, and S. M. Torres, 2013: Radial-based Noise Power Estimation for Weather Radars, *J. Atmos.Oceanic Technol*., 30, 2737–2753. Available at doi: http://dx.doi.org/10.1175/JTECH-D-13-00008.1

Ivić, I.R., and R. J. Doviak, 2016: Evaluation of phase coding to mitigate differential reflectivity bias in polarimetric PAR. *IEEE Trans. Geosci. Remote Sens., 54,* 431–451, Available at doi:10.1109/TGRS.2015.2459047.

Ivić, I. R., 2017: Phase Code to Mitigate the Copolar Correlation Coefficient Bias in PPAR Weather Radar. *IEEE Trans. Geosci. Remote Sensing, GE-55(4),* 2144-2166. Available at doi: https://doi.org/10.1109/TGRS.2016.2637720

Ivić, I. R., 2017a: An experimental evaluation of phase coding to mitigate the cross-coupling biases in PPAR. *38th International Conference on Radar Meteorology,* Chicago, IL. Available at: 10.13140/RG.2.2.28686.87362

Ivić, I. R., 2018: Options for Polarimetric Variable Measurements on the MPAR Advanced Technology Demonstrator, *IEEE Radar Conference (RadarConf18)*. Available at doi: https://doi.org/10.1109/RADAR.2018.8378544

Ivić, I. R., 2018a: Effects of Phase Coding on Doppler Spectra in PPAR Weather Radar. *IEEE Trans. Geosci. Remote Sensing, GE-56(4),* 2043 – 2065. Available at: https://doi.org/10.1109/TGRS.2017.2772962

Ivić, I.R., 2018b: On the Use of Horn Antenna to Calibrate the MPAR Advanced Technology Demonstrator. *10th European Conference on Radar in Meteorology and Hydrology*, Wageningen, Netherlands. Available at: https://www.researchgate.net/publication/326258272_On_the_Use_of_Horn_Antenna_to_Calibrate_the_MPAR_Advanced_Technology_Demonstrator

Ivić, I. R., 2019: Facets of Planar Polarimetric Phased Array Radar Use for Weather Observations. AMS 99th Annual Meeting, Phoenix, AZ. Available at: https://ams.confex.com/ams/2019Annual/webprogram/Paper350901.html

Ivić, I. R., and D. Schvartzman 2019: A first look at the ATD data corrections. Preprints, *39th International Conference on Radar Meteorology*, Nara, Japan. Amer. Meteor. Soc., Paper 2-06. Available at: https://cscenter.co.jp/icrm2019/program/data/abstracts/Poster2-06_2.pdf

Ivić, I. R., and D. Schvartzman 2020: Weather Calibration Efforts on the Advanced Technology Demonstrator, *American Meteorological Society 100th Annual Meeting*, Boston, 2020, Paper 8B.4. Available at: https://ams.confex.com/ams/2020Annual/meetingapp.cgi/Paper/363084

NOAA/NWS RFR 2015: NOAA/National Weather Service Radar Functional Requirements. Available at: https://www.roc.noaa.gov/WSR88D/PublicDocs/NOAA_Radar_Functional_Requirements_Final_Sept%202015.pdf

Ryzhkov, A. V., and D. Zrnić, 2019: Radar Polarimetry for Weather Observations. Springer, 486 pp.

Stailey, J. E., and K. D. Hondl, 2016: Multifunction phased array radar for aircraft and weather surveillance. *Proc. IEEE, 104*, 649–659. Available at: doi: https://doi.org/10.1109/JPROC.2015.2491179.

Zrnić, D. S., J. F. Kimpel, D. E. Forsyth, A. Shapiro, G. Crain, R. Ferek, J. Heimmer, W. Benner, T. J. McNellis, and R. J. Vogt, 2007: Agile beam phased array radar for weather observations, *Bull. Amer. Meteorol. Soc., 88(11)*, 1753-1766. Available at: https://doi.org/10.1175/BAMS-88-11-1753

Zrnić, D. S., V. M. Melnikov, and R. J. Doviak, 2012: Issues and challenges for polarimetric measurement of weather with an agile beam phased array radar. NOAA/NSSL Rep., 119 pp. Available at: http://www.nssl.noaa.gov/publications/mpar_reports/

Zrnić, D.S., R.J. Doviak, V.M. Melnikov, and I.R. Ivić, 2014: Signal Design to Suppress Coupling in the Polarimetric Phased Array Radar. *J. Atmos. Oceanic Technol., 31*, 1063–1077. Available at: https://doi.org/10.1175/JTECH-D-13-00037.1.

Weber, M. E., 2019: Meteorological Phased Array Radar Research at NOAA's National Severe Storms Laboratory. *2019 IEEE International Conference on Microwaves, Antennas, Communications and*

Electronic systems (COMCAS). Tel Aviv, Israel. Available at: doi: 10.1109/COMCAS44984.2019.8958067